

Thermal Drawdown-Induced Flow Channeling in Fractured Geothermal Reservoirs

Pengcheng Fu¹ · Yue Hao¹ · Stuart D. C. Walsh¹ · Charles R. Carrigan¹

Received: 31 March 2015 / Accepted: 1 June 2015
© Springer-Verlag Wien (outside the USA) 2015

Abstract We investigate the flow-channeling phenomenon caused by thermal drawdown in fractured geothermal reservoirs. A discrete fracture network-based, fully coupled thermal–hydrological–mechanical simulator is used to study the interactions between fluid flow, temperature change, and the associated rock deformation. The responses of a number of randomly generated 2D fracture networks that represent a variety of reservoir characteristics are simulated with various injection–production well distances. We find that flow channeling, namely flow concentration in cooled zones, is the inevitable fate of all the scenarios evaluated. We also identify a secondary geomechanical mechanism caused by the anisotropy in thermal stress that counteracts the primary mechanism of flow channeling. This new mechanism tends, to some extent, to result in a more diffuse flow distribution, although it is generally not strong enough to completely reverse flow channeling. We find that fracture intensity substantially affects the overall hydraulic impedance of the reservoir but increasing fracture intensity generally does not improve heat production performance. Increasing the injection–production well separation appears to be an effective means to prolong the production life of a reservoir.

Keywords Geothermal · Enhanced geothermal system · Hot wet rock · Thermal breakthrough · Flow channeling · THM model

✉ Pengcheng Fu
fu4@llnl.gov

¹ Atmospheric, Earth, and Energy Division, Lawrence Livermore National Laboratory, Livermore, CA 94550, USA

1 Introduction

Engineered (or enhanced) geothermal systems (EGS) are usually located in fractured rock formations, where the permeability of the intact rock matrix is very low and the inter-connected fracture network provides the primary conduit of fluid between the injection well(s) and the production well(s). Since heat conduction in the rock matrix is much slower than convective heat transfer associated with fluid flow along fractures, it is highly desirable to have flow patterns dispersed throughout a large volume of rock. The understanding of flow patterns in EGS reservoirs plays a critical role in the optimization of reservoir exploration, stimulation, and operation.

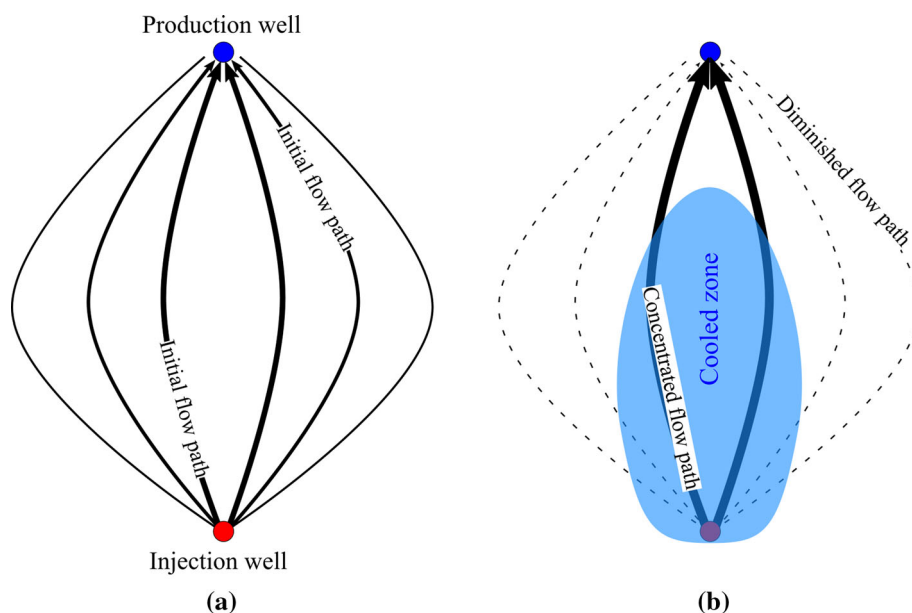
The term “flow channeling” generally refers to concentration of the flow network in a relatively small number of “flow channels” or “flow pathways”, as opposed to evenly dispersed flow in the medium. In the context of flow in fractured media, its meanings are manifold. When fluid flow along a given single fracture is concerned, “flow channeling” is used to describe the distinctive linear channels forming along this planar fracture (Tsang and Tsang 1987; Tsang and Neretnieks 1998; Auradou et al. 2006). In the reservoir scale involving a network of fractures, “flow channeling” refers to a flow pattern in which a small portion of the fractures carry the majority of the fluid flow. The primary reason for channelized flow in these two cases is the heterogeneous spatial distribution of fracture transmissivity, along a given fracture plane and within the fracture network, respectively. “Flow channeling” also refers to the process through which a channelized flow pattern forms or evolves due to various mechanisms.

The present study focuses on the evolution of flow channeling at the reservoir scale associated with thermal drawdown in EGS. An intuitive mechanism for this process

is illustrated in Fig. 1 as follows: at the commencement of the production phase of an EGS (before significant thermal drawdown has taken place), the flow pattern from the injection well(s) to the production well(s) is likely to be somewhat channelized, owing to the inherent heterogeneity of the fracture system (i.e. the second phenomenon described in the previous paragraph). The thicker and thinner lines in Fig. 1a represent flow paths with higher and lower flow rates, respectively. During heat production, fractures that carry higher flow rates are likely to cool faster. Thermal stress in the cooled rock (the blue zone in Fig. 1b) is typically a tensile increment in addition to the original compressive in situ stress. It tends to reduce the magnitude of the total compressive stress on fractures inside the cooled rock, thereby increasing the permeability along these fractures. Therefore, a likely scenario is that flow will further concentrate in these cooled fractures and diminish in others as shown in Fig. 1b. This is undesirable for EGS because it reduces the effective heat exchange area of the reservoir and undermines long term thermal performance. This mechanism has been demonstrated by numerical models, such as those in Hicks et al. (1996), DuTeaux et al. (1996), and Koh et al. (2011). It has been observed in several EGS projects that the overall flow impedance between the injection and production wells decreases with heat production (Kohl et al. 1995), which could be a manifestation of the hypothetical mechanism. However, tracer tests at the Fenton Hill EGS site indicated that the flow pattern became more diffuse at certain stages of the heat production operation (DuTeaux et al. 1996). Flow channeling, particularly the mechanisms of flow channeling, in EGS during heat production deserves further investigation.

The phenomenon to be studied herein entails coupled mechanical, hydrological, and thermal processes. Hence, the numerical model must simulate all the three aspects of the problem and their coupling. Various coupled thermal–hydrological–mechanical (THM) models and models coupling two of the three aspects for geothermal reservoirs have been developed and reported in the literature. Models for conventional geothermal resources, namely hydrothermal systems dominated by flow in porous rock formations, typically handle fluid and heat flow using porous medium flow theories (see a review in O’Sullivan et al. 2001). Mechanical coupling capability can be added to these models through rock constitutive models based on continuum mechanics, which quantifies the stress–strain relationship of the porous medium (Hart and St. John 1986; Rutqvist et al. 2002; Taron et al. 2009; Taron and Elsworth 2009). For EGS reservoirs dominated by flow in fractures, the porous medium models have been found to be inadequate (Nicol and Robinson 1990), and explicit representation of the fracture system is necessary. A number of models in the literature focus on the flow and deformation of a single fracture. Such models could be useful for reservoirs that are dominated by a single fracture (Bödvarsson and Tsang 1982; Ghassemi et al. 2007). Several coupled THM models based upon discrete fracture network (DFN) flow have been developed. The early models usually handle simple fracture network patterns whereas the more advanced ones can deal with random fracture networks. Many complex and interesting phenomena in EGS reservoirs have been revealed by the application of these models, but a comprehensive study of thermal drawdown-induced flow channeling is still missing.

Fig. 1 Conceptual illustration of the flow channeling concept in an idealized fracture network: **a** the flow field in the initial state, and **b** the flow field after a cooled zone has developed due to heat production. The solid arrowed line represents flow paths with the flow rate denoted by the line thickness



We present a fully coupled THM model for fluid and heat flow in discrete fracture networks and use the model to gain insight into the flow channeling phenomenon associated with thermal drawdown. Despite the decades of effort since the Fenton Hill experiment, EGS research is still in the concept-validation phase and only a small number of experimental sites have been developed so far (see reviews in Jung 2013; McClure and Horne 2014). The objective of the current study is to reveal physical mechanisms governing the flow-channeling process through the study of a set of reasonable synthetic reservoir configurations, and to provide practically useful guidance for the development and operation of EGS. We focus on behavior of hot-wet-rock (HWR) geothermal systems (Willis-Richards et al. 1996), where the natural fracture network provides the majority of the permeability and the reservoir is saturated with water in its natural state.

2 Coupled THM Model

2.1 Modeling Strategy

Our strategy for modeling coupled THM processes in the production phase of EGS reservoirs is based on the following considerations and assumptions:

- Matrix permeability of the rock formation is ignored and all fluid flow is through the discrete fracture network.
- Fluid pressure is lower than the “jacking” pressure, namely the minimum in situ principal stress (effective stress, compression is positive) in the rock formation. In this pressure regime, the change of fluid pressure in fractures only induces minimal change of the stress state in the surrounding rock matrix (Fu et al. 2012). Therefore, the interaction between neighboring fractures through a “stress shadowing” effect (Kresse et al. 2013) is insignificant and ignored in our model. Because fractures in this pressure regime are still closed, we consider the solid phase in the reservoir as a continuum for the calculation of thermal stress.
- Thermal drawdown in EGS reservoirs is a relatively slow process. Field observation and numerical modeling have both indicated that its effect on reservoir behavior is only noticeable over a time scale of months (Bruehl 2002). We assume that the flow field is in a steady state within each time step. We use a time step that is sufficiently small so that the simulation results are insensitive to further reduction of the time step size.
- The simulations are performed in two-dimensional (2D) space under plane-strain conditions. The 2D model can be considered as a horizontal cut through a rock body containing steeply dipping fractures in the

normal stress regime (i.e. vertical stress is the major principal component). Although it is well recognized that many characteristics of random fracture networks cannot be adequately represented by 2D models, and the quantitative values from 2D models should not be directly used for real world projects, we can still use 2D models to gain insight into the physical processes governing EGS reservoir performance, which would be very useful for optimizing stimulation and production strategies. Results of 2D models also inspire the development of more sophisticated 3D models (Fu et al. 2013; Settgast et al. 2012).

The numerical model consists of four main modules as illustrated in Fig. 2. We briefly describe the framework of the numerical method and discuss the coupling strategy between different modules. The details of each module are provided in subsequent sections.

In each time step, a rock joint model and a DFN-based fluid flow solver are first invoked iteratively to calculate the steady-state flow field in the fracture network. In this paper, the word “joint” is used as a generic term referring to any uncemented discontinuity in rock formations in a similar fashion to Cook (1992). In each iteration, the flow solver determines the pressure distribution within the fracture network for the given aperture width distribution and boundary conditions. The rock joint model then returns the aperture width of each flow element for the next iteration, determined by a function of the local total stress, the fluid pressure provided by the flow solver, and the intrinsic joint characteristics at each fracture segment. Once these iterations converge, we obtain a fracture transmissivity field and a flow field that are consistent with the given stress boundary conditions, flow boundary conditions, and rock joint characteristics for the current time step. Figure 3a shows a random DFN and Fig. 3b shows the flow rate field near the injection well solved by the DFN model where the direction and width of the black triangles denote the flow direction and flow rate, respectively.

Next, we use a porous medium-based heat and flow transport model (i.e. a TH flow model) to advance the temperature field for the present time step. To this end, we

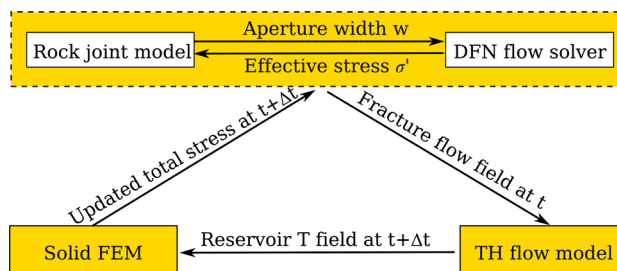


Fig. 2 Main modules of the coupled THM model. Symbols t , Δt , and T denote time, time increment, and temperature, respectively

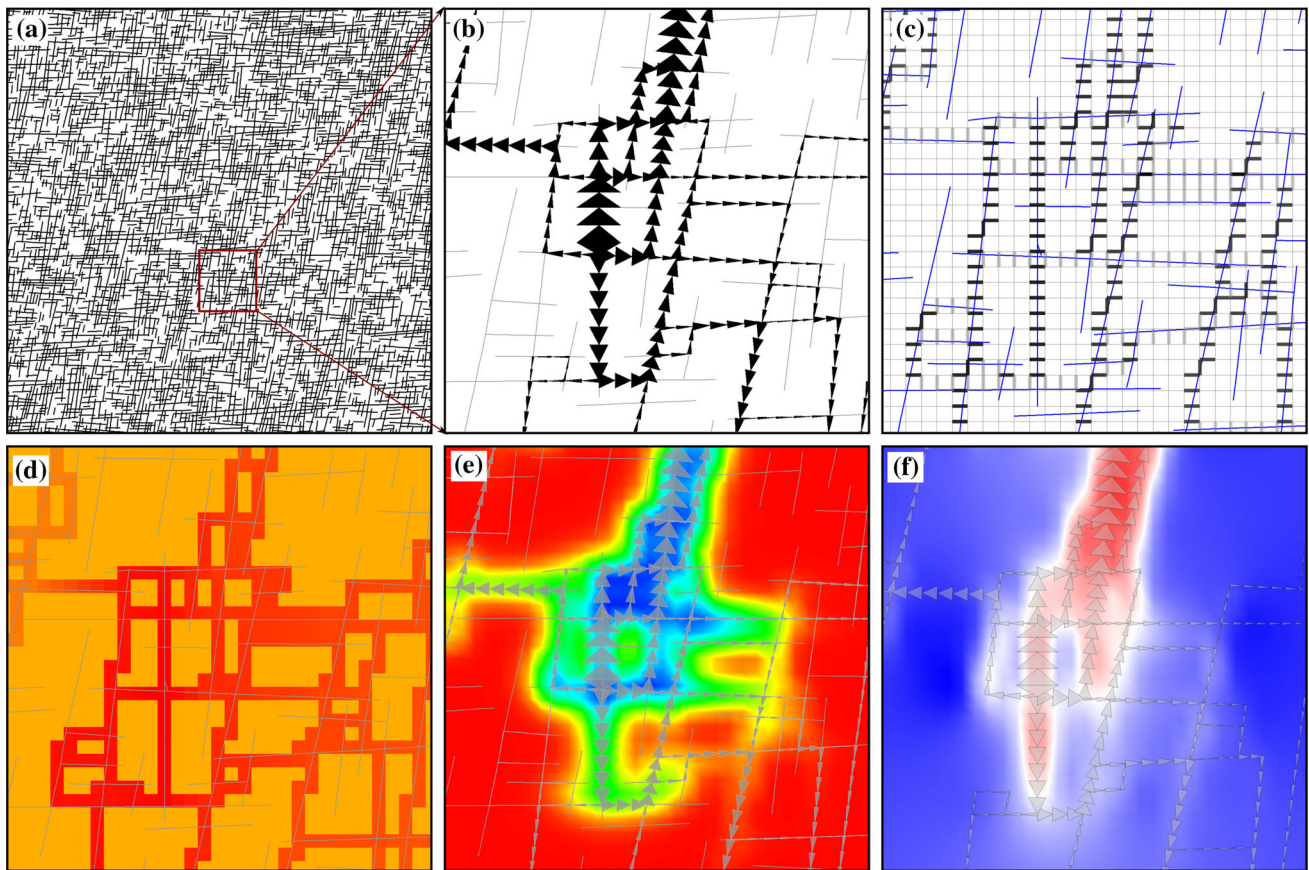


Fig. 3 The mapping of variables used by different modules of the coupled model. **a** A random discrete fracture network. **b** The flow field near the injection well in the DFN model after 3 years of injection. **c** The regular Cartesian grid used by the porous medium model overlaid on the DFN. The DFN elements are shown in *thin blue lines*. The *darkness (gray to black)* of the thickened cell–cell interface lines quantifies the transmissivity between adjacent cells, with *darker color* denoting greater transmissivity. **d** Pressure field in the Cartesian grid solved by the porous medium model. High pressure cells are

map the DFN-based transmissivity field onto the permeability field of a regular grid used by the porous medium model. The fluid flow solution obtained by the TH flow model is equivalent to that obtained by the DFN flow solver. The flow solution is used to calculate the heat transfer between the solid phase and the fluid phase, as well as the convective heat transport along the fractures. At the end of the time step, the reservoir temperature field is obtained from the TH flow model, and mapped onto a finite element method (FEM) solid mesh for calculation of the thermal stress. Finally, we update the total stress on each fracture segment used in the DFN flow module and start the next time step. The time increment for a whole cycle shown in Fig. 2 is 4 months for all the simulations presented. We found that further reducing cycle duration did not significantly alter the simulation results. Note that each cycle involves many (typically hundreds of) time steps of the porous medium solver.

shown in *red* and unpressurized solid medium is in *yellow*. **e** The temperature field (*red* denotes high temperature and *blue* low temperature) solved by the porous medium model. **f** The thermal stress (*yy* component; tensile stress in *red* color and compressive in *blue*) field solved by the solid finite element model. These figures only conceptually illustrate the mapping of variables between meshes/models, so the color tables are not provided (color figure online)

2.2 DFN Flow Solver

The DFN flow solver uses a simple FEM formulation based on two-node line elements. In two-dimensional space, discrete fractures are geometrically represented by line segments, and each fracture is discretized into line elements of approximately equal lengths. Intersection points between fractures have to be represented by nodes, which imposes an additional constraint on the discretization of the fractures. According to the parallel plate laminar flow assumption, the flow rate through a flow element between node i and node j is

$$Q_{ij} = \frac{(P_i - P_j)w^3}{12l_{ij}\mu_F} \quad (1)$$

where P_i and P_j are the fluid pressure at two adjacent nodes; l_{ij} is the length of the element; μ_F is the dynamic viscosity of the fluid; and w is the aperture width, which

will be discussed in Sect. 2.3. A global system of governing equations is established by enforcing the mass conservation condition that the net flow into each node is balanced by the net flow out.

2.3 Rock Joint Model

The closure behavior of a fracture, namely the variation of the aperture width w with respect to the effective stress σ' is often characterized by joint models in rock mechanics, of which the Barton-Bandis model (Bandis et al. 1983; Barton et al. 1985) is a classical example. The model states

$$\sigma' = \frac{w_{\max} - w}{a_J - b_J(w_{\max} - w)}, \quad (2)$$

where σ' is the effective compressive stress, i.e. the difference between the total normal stress σ_n acting on the fracture and the fluid pressure P within the fracture; w_{\max} is the aperture width at the zero-effective stress state, which is essentially the maximum joint closure in the original joint model of Bandis et al. (1983); a_J and b_J are two material- and state-specific constants. This constitutive model for rock joints has been widely used in various numerical models for fracture-dominated geothermal reservoirs (Kohl et al. 1995; Bower and Zyvoloski 1997; Bruel 2002). If we identify a second reference state with effective normal stress σ'_{ref} and the corresponding aperture width w_{ref} , the two material constants can be calculated as

$$a_J = w_{\max} \frac{w_{\max} - w_{\text{ref}}}{\sigma_{\text{ref}} w_{\text{ref}}} \quad \text{and} \quad b_J = w_{\max} \frac{w_{\max} - w_{\text{ref}}}{\sigma_{\text{ref}} w_{\text{ref}}}. \quad (3)$$

In our previous work (Fu and Carrigan 2012), we have proposed to use parameters a_J and b_J as state variables to reflect the effects of shear dilation on closure behavior of rock joint. Since we focus on the production phase instead of the stimulation phase of the reservoir, the two state variables are constants for all fracture elements in the current study. Note that the aperture width of individual fracture segments can still vary based on the total stress and fluid pressure.

2.4 Modeling Heat Transfer Using an Effective Porous Medium Model

Heat transfer in the fractured reservoir is simulated using a dual-continuum model implemented in a porous medium-based flow and transport code NUFT (Nonisothermal Unsaturated-saturated Flow and Transport). NUFT is based on Darcy's flow approximation and models multiphase, multi-component heat and mass flow and reactive transport in unsaturated and saturated porous medium (Nitao 1998; Hao et al. 2012). The formulation and verification of the dual-continuum model have been detailed in

Hao et al. (2013) and are not repeated here. In this section, we present the procedure of converting the flow field obtained by the DFN-based model to that on a regular Cartesian grid used by NUFT.

Because the heat flow in fractured geothermal reservoirs is closely associated with fluid flow in the medium, we have to create a flow field that is consistent with that obtained by the DFN-based solver and compatible with the regular Cartesian grid used by NUFT. We developed a method similar to the "fracture continuum" method proposed by Botros et al. (2008) and Reeves et al. (2008) and overlay the DFN-based fracture elements onto the Cartesian grid used by NUFT as shown in Fig. 3c. In NUFT, the permeability field is represented by the conductivity between any two adjacent cells. In the two overlaid meshes, if a fracture element geometrically intersects the interface (a line segment in 2D) between two adjacent porous medium cells in the regular grid, this fracture segment's contribution to the conductivity between these two cells is

$$\Delta k = \frac{C(\theta)w^3}{12A} \quad (4)$$

where k is the permeability of the porous medium according to Darcy's law; A is the area (length in 2D) of the interface between the two cells; θ is the angle between the fracture element and the Cartesian grid axis; and $C(\theta) = |\sin\theta| + |\cos\theta|$, is a correction factor to compensate for the longer flow paths in the Cartesian grid than the corresponding length of the fracture. This mapping is illustrated in Fig. 3c, where the darkness of the thickened cell-cell interface lines denotes the transmissivity between these two cells. The permeability of an inter-cell interface can be contributed to by multiple fractures and the principle of superposition applies. Only the fracture elements that carry non-zero flow are included in the mapping, and that is why most of the cell-cell interface lines are not thickened, even though many of them are intersected by fractures that do not carry flow. This is an advantage of our proposed method compared to the fracture continuum method (Botros et al. 2008; Reeves et al. 2008) in which a similar mapping is carried out. In the latter the DFN are pure geometrical entities and the flow field is only solved by the porous medium solver. If the Cartesian grid spacing is comparable to or greater than discrete fracture spacing, false transmissivity can be generated by discrete fracture segments that do not carry flow, a well known phenomenon that causes over-prediction of flow (Botros et al. 2008; Reeves et al. 2008). By ignoring DFN elements that do not carry flow, our method maps the actual "flow field" solved by the DFN solver instead of mere DFN geometries. Therefore, the flow field solved by the porous medium solver is nearly identical to the DFN flow field and the

results are insensitive to the resolution of the Cartesian grid.

To continue the example illustrated by Fig. 3a–c, Fig. 3d shows the pressure field solved by the porous medium solver and Fig. 3e shows the temperature field evolved by NUFT. Additionally, an example of a DFN-based flow field and its equivalent representation with a regular grid is presented in Fig. 13 along with the numerical examples in Sect. 4.2.

2.5 Calculation of the Thermal Stress

As discussed in Sect. 2.1, we treat the rock body containing closed fractures as a continuum for the calculation of thermal stress. The finite element mesh for this purpose can be established independently. We map the temperature field onto the continuum FEM mesh at the center of each element. The thermal stress field is calculated following the procedure outlined in Sect. 2.10 of Cook et al. (2001). The approach is a standard method employed in thermo-mechanical finite element analysis and not repeated here. The thermal stress (yy-component) corresponding to the temperature field in Fig. 3e is shown in Fig. 3f.

Initially, the fluid pressure is lower than the minimum principal in situ stress, ensuring that all fractures are closed. Over time, however, changes in the thermal stress can reduce the total stress in the rock to the extent that some fractures open due to the contraction of surrounding rock. In this situation, the aperture size cannot be determined by the joint model in Sect. 2.3 and ideally should be calculated with a fully coupled model, such as that of Fu et al. (2013), with open fractures explicitly meshed in the FEM model. For all of the simulations in the present paper, this condition only occurs within a limited area near the injection well. When these fractures (usually a small number) open, the flow rate is determined by the closed fractures that are connected to these open fractures, and thus the transmissivity of the open fractures has minimal effect on the overall flow field. Therefore, we assign a large value, for instance $2w_{\max}$ to the aperture width of opened fractures.

The three main modules in the numerical model use three distinct meshes: the DFN solver uses an FEM mesh composed of two-node line elements; NUFT uses a regular Cartesian grid; and the thermal stress module uses a solid mechanics FEM mesh. The three meshes do not need to conform with each other as long as variable mapping between meshes is correctly handled. In all the simulations presented, the minimum distance between any two sub-parallel fractures is 10 m, and the resolutions for the DFN models, NUFT models, and the thermal stress FEM models are all approximately 8 m, unless explicitly specified otherwise.

3 A Highly Idealized Baseline Case

In this section, we study a reservoir with a highly idealized fracture system as the baseline case, which enables us to identify expected common behavior of fractured geothermal reservoirs, as well as a new mechanism that counteracting the flow channeling mechanism described in Sect. 1.

3.1 Model Setup

The idealized reservoir consists of two orthogonal fracture sets forming a regular grid as shown in Fig. 4. A 2D coordinate system is established so that the x -axis points east and the y -axis points north. We term the fracture set parallel to the x -axis the “ x -set” and the other the “ y -set”. The domain, as well as the fracture network, is assumed to be infinite, and the numerical model is made large enough to minimize the effects of far-field boundaries. Fracture spacing for both sets is 20 m. The in situ stress components are $\sigma_x = \sigma_h = 18$ MPa and $\sigma_y = \sigma_H = 25$ MPa, where σ_h and σ_H are the minimum and maximum horizontal principal stresses, respectively. Note that σ_x happens to be the normal stress acting on the y -set and σ_y acts on the x -set. The production well is 600 m north of the injection well, and each well is at an intersection of two fractures. The original natural fluid pressure in the fracture system is 15 MPa, and the pressure boundary condition at the far-field boundary is fixed at this value. The resolution of the

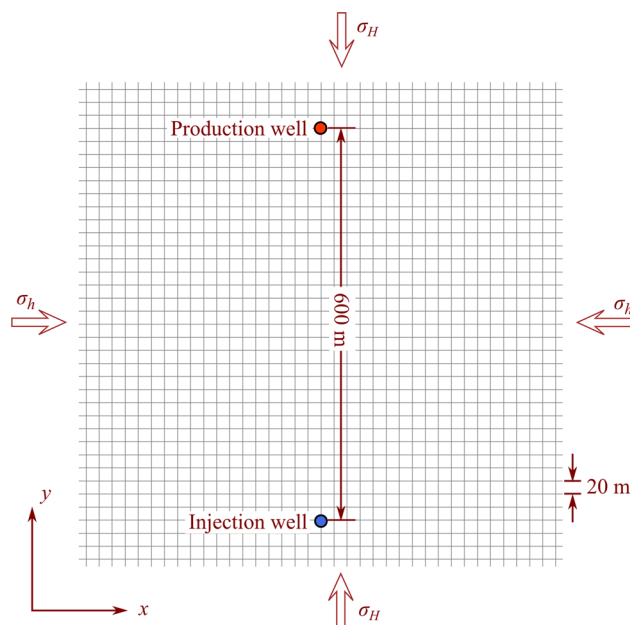


Fig. 4 Layout of the idealized reservoir consisting of two infinite orthogonal fracture sets. Note that only the center portion of the numerical model is shown. In all the layout maps in the present paper, the locations of the *injection well* and the *production well* are denoted by *small circles*

DFN mesh is 4 m. Some other important parameters are shown in Table 1. Note that properties of real water are functions of the water’s state such as temperature and pressure. Using constant properties introduces certain amount of error in the calculated results, mainly in calculated the pressure loss. However, since the main phenomenon investigated by the current study, namely flow channeling associated with reservoir temperature drop, is caused by thermal–mechanical coupling that is independent of water property change, these constant properties are not expected to affect the comparison between the scenarios investigated herein.

Although we use the same rock joint parameters for the two joint sets, their initial apertures are affected by the anisotropic in situ stress and thus not the same. According to the joint model described by Eq. (2), the aperture widths for the x-set and y-set with zero-fluid pressure are 0.066 and 0.082 mm, respectively. The y-set has significantly higher hydraulic transmissivity than the x-set, which is the primary reason for the north–south well layout. We term the y-set fractures the primary set and the x-set the secondary set.

3.2 Pumping Pressure—Circulation Rate Response of Reservoir Before Thermal Drawdown

For all the simulations in the present paper, we use flow rate–controlled boundary conditions at the two wells. The injection rate is fixed at the same value as the production rate, emulating a common circulating strategy used in existing EGS sites (Genter et al. 2012, 2013; Hogarth and Bour 2015). To determine an appropriate flow rate, we run a series of simulations at different circulation rates and obtain the injection and extraction pressure required as

shown in Fig. 5. Note that all pressures presented in the current paper are the pressure at the reservoir depth. The results indicate that a higher circulation rate would require higher injection pressure and lower extraction pressure (higher net extraction pressure or stronger “suction”), as expected. Both curves are nonlinear, especially the extraction curve, which reflects the fact that as we increase the net extraction pressure (the absolute difference between the extraction pressure and the far-field pore pressure) the aperture near the extraction well decreases and the system hydraulic impedance increases. This implies that with increased pressure significantly more pumping power is required for the same amount of marginal increase of circulation rate. Based on the results, we choose 20 liters per second per 100 m thick reservoir (L/s/100 m) as the circulation rate at an initial injection pressure of 16.5 MPa and an initial extraction pressure of 9.7 MPa for the analysis in the rest of Sect. 3. Since 9.7 MPa is the hydrostatic pressure at approximately 1 km depth, a downhole pump would be required if the reservoir is deeper than 1 km.

3.3 Reservoir Behavior Without Thermo-Mechanical Effects

Figure 6 shows the flow field obtained by the DFN solver at the beginning of the production phase (i.e. no significant temperature change in the reservoir has occurred). In this figure and all subsequent figures quantifying DFN flow fields, we use the orientation and width of the gray triangles to denote the flow direction and flow rate, respectively. Assuming 100 m thick reservoir, a fracture flow rate of 1.0 L/s is corresponding to a triangle 2.4 m wide. The scale of flow visualization, i.e. the ratio of triangle width to fracture flow rate is the same for all plots in the current

Table 1 Model parameters for the idealized baseline simulation

Parameter	Value
Original in situ stress	$\sigma_x = \sigma_h = 18$ MPa (east–west) $\sigma_y = \sigma_H = 25$ MPa (north–south)
Original pore pressure	$P_0 = 15$ MPa
Rock joint parameters	$w_{max} = 1.0$ mm $\sigma_{ref} = 20$ MPa $w_{ref} = 0.08$ mm
Initial reservoir temperature	$T_0 = 150$ °C
Injection fluid temperature	$T_i = 50$ °C
Mechanical properties of rock	Young’s modulus $E = 20$ GPa Poisson’s ratio $\nu = 0.2$ Linear thermal expansion coefficient $\alpha_L = 8 \times 10^{-6}$
Thermal properties of rock	Thermal conductivity $K_r = 3$ W/m/°C Heat capacity $C_r = 2.5$ MJ/m ³ /°C
Fluid properties	Dynamic viscosity $\mu_f = 0.001$ Pa s Heat capacity $C_f = 4.2$ MJ/m ³ /°C

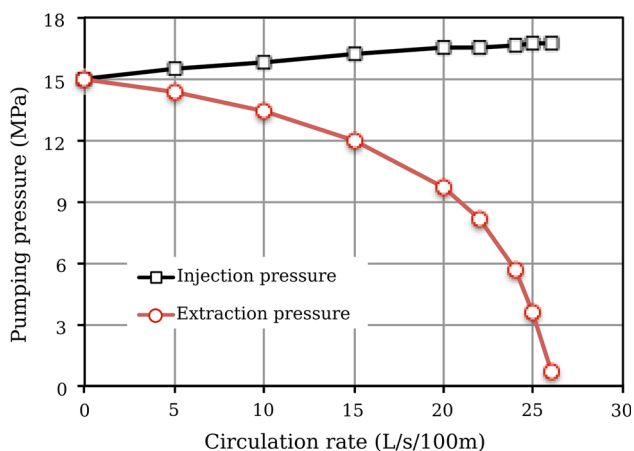


Fig. 5 Pumping pressure—circulation rate relationship of the idealized reservoir. The unit of circulation rate is liter per second for a 100 m thick reservoir. The pressure is that at the intersection between the wellbores and the reservoir

paper. A few y-set fractures near the center of the domain carry the majority of the flow. In this region, the flow rate in the y-set fractures is substantially higher than in the x-set fractures, because the total stress on y-set is lower than that on x-set, resulting in wider apertures. However, because only one fracture in the y-set is directly connected to the two wells, flow in all the other y-set fractures must be “fed” by x-set fractures intersecting with them. Therefore, the low conductivity of the x-set fractures is the main reason why more dispersed flow patterns cannot form under the given conditions. We term the flow along the

y-direction the primary flow and that along the x-direction the secondary flow. Clearly, flow in both directions is needed to form a flow network. Also note that there is a significant amount of fluid injected into the reservoir flows along the negative y-direction, i.e. the direction away from the production well. Figure 6b shows that such “runaway” flow is gradually diverted by x-set fractures, and it eventually reaches the production well through peripheral flow channels. The flow into the production well that originates from the far-field (as shown in Fig. 6c) is caused by the same mechanism. In this paper, we refer to such flow as “peripheral flow”. The aforementioned behaviors of the flow network are clearly illustrated by Fig. 7, where flow diversion and merging have caused discontinuity in the flow rate along the two fractures shown, at $x = 0$ and $x = 60$ m, respectively.

If we disregard the thermo-mechanical (TM) effects on flow channeling, we can directly use NUFT to simulate the temperature field evolution in the reservoir without requiring the full procedure shown in Fig. 2. The results provide a useful baseline reference for the study of flow pattern changes due to TM effects. The evolution of production temperature for this scenario is shown in Fig. 8 as a solid line, and the reservoir temperature fields 5, 10, 20, and 30 years into the production phase are shown in Fig. 9. According to the simulation results, the cooling front arrives at the production well in less than 5 years of production. The production temperature gradually decreases afterwards and is approximately 98 °C after 30 years of production.

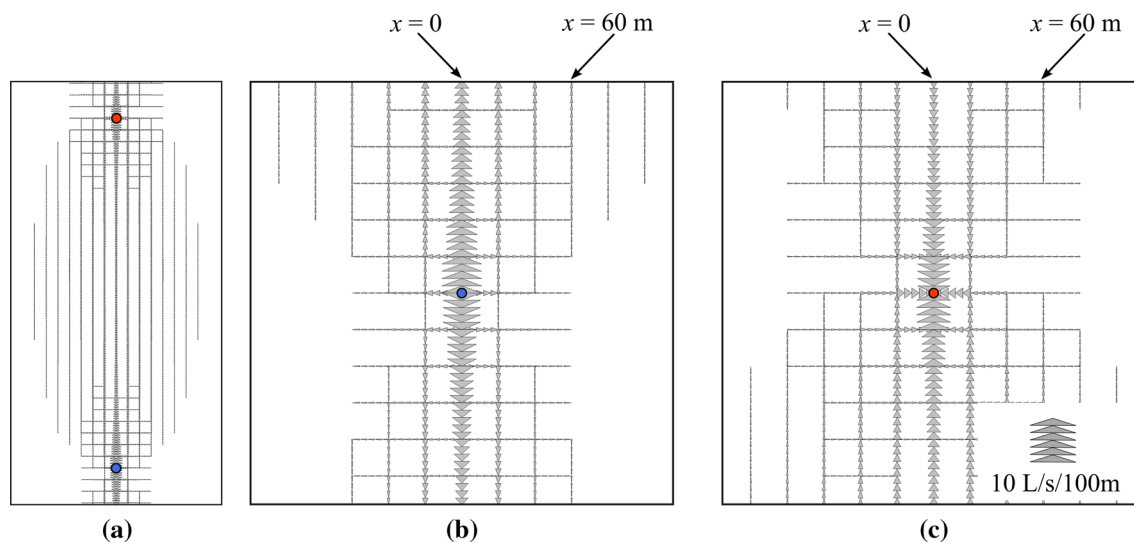


Fig. 6 Initial flow field in the idealized reservoir. The direction and width of the gray triangles denote the flow direction and flow rate, respectively. Assuming 100 m thick reservoir, a fracture flow rate of 1.0 L/s is corresponding to a triangle 2.4 m wide. This ratio applies to all flow rate visualizations throughout the paper wherever applicable.

The simulation domain is 1600 m × 1600 m and not fully shown. Fractures with flow rates smaller than 0.2 L/s are not shown. **a** The domain enclosing the two wells; **b** magnifies the region around the injection well; and **c** magnifies the region around the production well

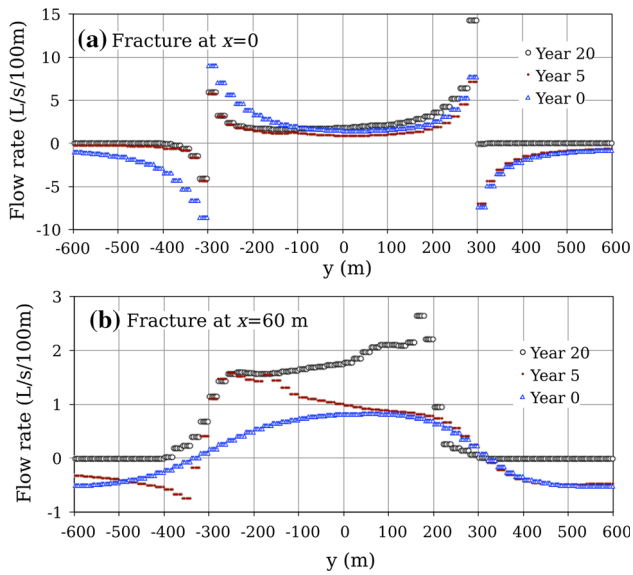


Fig. 7 Flow rate along two y -set fractures, one at **a** $x = 0$ and the other one at **b** $x = 60$ m as marked in Fig. 5. The injection well is located at $x = 0$, $y = -300$ m and the production well at $y = 300$ m. Flow along the positive direction of the y -axis is considered to have a positive flow rate and against this direction negative. Flow rate along each straight fracture is continuous within each 20 m segment between intersections but appears discontinuous due to the diversion of flow to or from the x -set fractures

3.4 Coupled THM Simulation Results

If we invoke the THM coupling loop shown in Fig. 2, the flow pattern will evolve with the temperature field. The production temperature history obtained by the coupled simulation is shown as the dotted line in Fig. 8. Snapshots of the temperature and flow fields are shown in Fig. 10.

By comparing the temperature and flow fields between Figs. 9 and 10 at year 5, we see that the TM effects tend to divert flow from the center fracture in the y -set, which directly connects the two wells, to a few y -set fractures

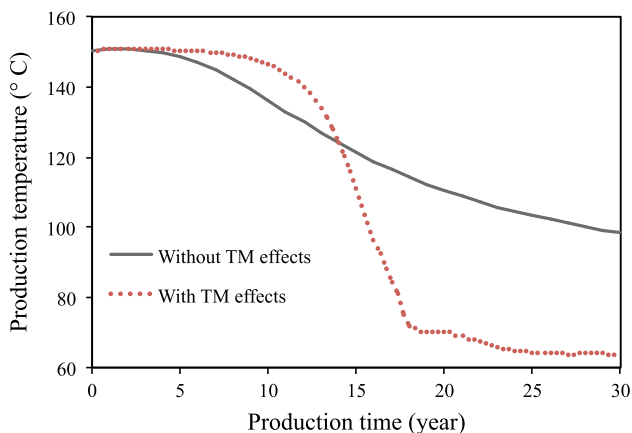


Fig. 8 Evolution of fluid temperature at the production well for the idealized reservoir

running parallel to the center fracture. This causes a slightly more diffuse flow pattern. This phenomenon is also evident in Fig. 7: after 5 years, the flow rate in the fracture at $x = 0$ m between $y = -300$ m and $y = -200$ m is substantially lower than the initial state; and in the fracture at $x = 60$ m flow rate has significantly increased in the first 5 years. This trend is also consistent with the observed response of the temperature field: when the TM effects are considered, the cooled zone is wider and the cooling front's propagation toward the projection well is slightly slower.

The TM effects substantially impede peripheral flow (defined in Sect. 3.3) in the reservoir. After 20 years, flow is almost completely concentrated in the cooled rock volume. This is one of the factors contributing to the fast decrease of production temperature after thermal breakthrough. In the scenario ignoring TM coupling, nearly half of the flow into the production well is through peripheral flow channels, and this portion of the fluid is not affected by the cooling of the interior reservoir. Therefore, the fluid extracted from the production well is indeed a mix of the relatively cold fluid from the interior flow and the hot fluid from the peripheral flow. On the other hand, because TM coupling impedes peripheral flow, the flow into the production well is primarily through the cooled reservoir, so the production temperature declines rather rapidly. Due to the same mechanism, the cooled zone extends quite far in the negative y -direction if TM coupling is ignored, while this extension is impeded when the full TM coupling is considered.

3.5 Anisotropic Thermal Stress and its Implication for Flow Channeling

We observe in Figs. 9 and 10 that the cooled zone in the reservoir elongates along the primary flow direction because of the fast cooling of rock adjacent to the fractures that carry high flow rate. Understanding of the anisotropy in thermal stress caused by this elongated cooling geometry is critical for gaining insight into the TM effects on flow channeling. To this end, we consider an idealized case for which closed-form solutions for thermal stress are available. This infinite 2D medium (plane-strain) has homogeneous physical and mechanical properties except that the temperature of an elliptical zone is ΔT lower than that of the rest of the medium, as illustrated in Fig. 11. The two principal axes of the ellipse align with the two coordinate axes, respectively, and the dimensions are $2a$ along the x -direction and $2b$ along the y -direction. Thermal stress develops in this cooled zone as well as in the medium surrounding it as a result of the cooling. The thermal stress inside the cooled zone is homogeneous, which can be calculated using our finite element model and can also be calculated using the following equations, which are

Fig. 9 Reservoir temperature distribution in the idealized reservoir if thermo-mechanical effects are ignored. The flow field is overlaid onto the temperature field but it does not evolve over time since the THM coupling is disabled

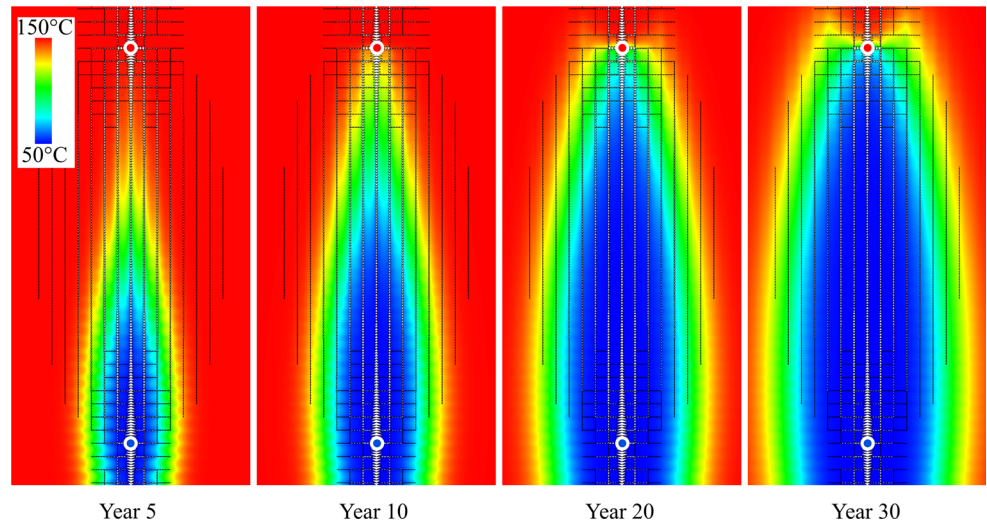
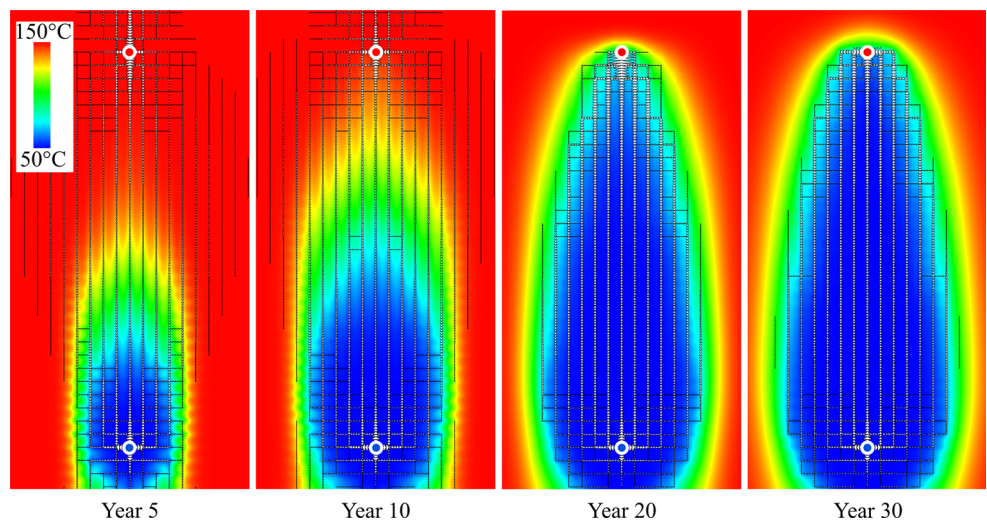


Fig. 10 Reservoir temperature distribution in the idealized reservoir if thermo-mechanical coupling is engaged. The flow field is overlaid onto the temperature field and evolves over time along with the temperature field evolution



simplified forms of the solution provided by Mindlin and Cooper (1950):

$$\sigma_x^T = \frac{-aE\Delta T\alpha_L}{(a+b)(1-\nu)}, \tag{5}$$

$$\sigma_y^T = \frac{-bE\Delta T\alpha_L}{(a+b)(1-\nu)}, \tag{6}$$

where E is the Young’s modulus of the medium; ν is the Poisson’s ratio of the medium; and α_L is the linear thermal expansion coefficient. Both normal components are tensile, which result in the negative sign. The ratio of the magnitude of the two thermal stress components (σ_x^T/σ_y^T) happens to be the aspect ratio of the ellipse. Note that closed-form solutions for thermal stress are only available for such a highly idealized case. Thermal stress for all the cases in the current paper is calculated using coupled thermal–mechanical finite element analysis.

Although the shape of the cooled zones shown in Figs. 9 and 10 is not exactly elliptical and the temperature in the cooled zone is not uniformly distributed, the anisotropy in thermal stress, shown in Fig. 12, resembles that of the elliptical cooled zone scenario to some extent. Therefore, the thermal stress along the primary flow direction (i.e. y-direction) is substantially greater (in absolute magnitude) than that along the secondary flow direction. Since thermal stress in the cooled zone is tensile and it tends to reduce the total normal stress (compressive) on fractures, the anisotropic thermal stress opens the secondary fracture set (the x-set) more than it does the primary set. As discussed in Sect. 3.3, this results in a more diffuse flow pattern, and thus flow must be fed into more primary set fractures through secondary set fractures. However, under anisotropic in situ stress, the secondary set acts as a bottleneck in the system and prevents highly diffuse flow patterns from forming. The anisotropic thermal stress is likely to

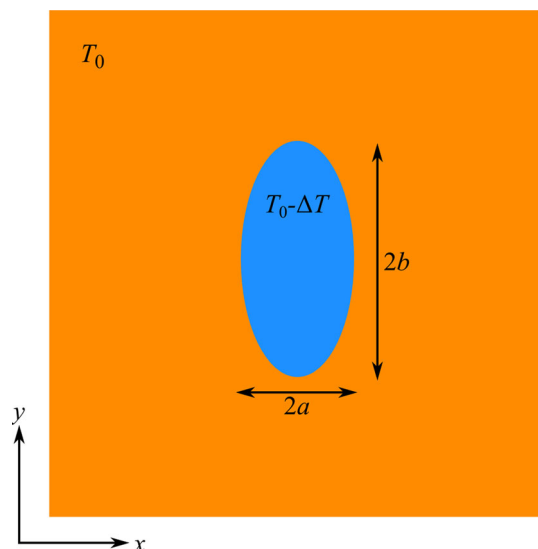


Fig. 11 Geometry of an *elliptical-shaped* cooling zone in an infinite medium. The analytical solution for the thermal stress in the cooling zone demonstrates the relationship between the shape of the cooling zone and the anisotropy of the thermal stress

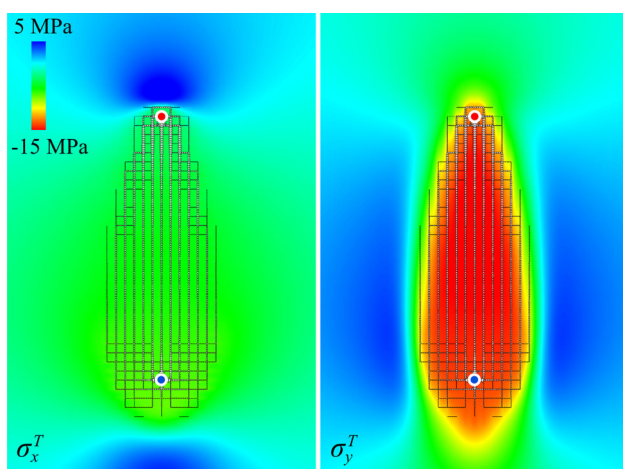


Fig. 12 Thermal stress in the idealized reservoir after 20 years of production. Compressive stress increment is positive

counteract the anisotropic in situ stress and enhance the conductivity of the secondary set fractures. This is the main reason for the more diffuse flow pattern and wider cooled zone in Fig. 10 than those in Fig. 9.

In Fig. 12 we also observe significant compressive thermal stress (denoted by the blue regions) develops along the periphery of the reservoir. This compressive stress increment tends to further compress the fractures around the cooled reservoir, which is an important mechanism that impedes peripheral flow.

In summary, the analysis of the highly idealized reservoir reveals the primary effect of TM coupling: it causes more open fractures inside the cooled reservoir and tighter fractures in the exterior compared with the initial states.

The combined effect is that flow tends to channelize inside the cooled reservoir, inducing rapid temperature decreases once thermal breakthrough has taken place. As a secondary effect, the anisotropy in the thermal stress increment tends to open the secondary set more than it does the primary set, which encourages a more diffuse flow pattern well before thermal breakthrough takes place, at least for fracture networks with intensive interconnectivity. This effect can delay thermal breakthrough.

4 Behavior of Random Fracture Networks

In this section, we investigate the THM responses of reservoirs with various fracture network patterns and well spacing. In real world reservoirs, natural fractures were created by a variety of geophysical and geological processes in rock formations. Certain characteristics of the natural fracture system in a given formation can be quantified, at least to some extent, through observations on formation outcrops and wellbore logs (e.g. Engelder et al. 2009), but such knowledge is generally scarce. Therefore, we investigate a number of artificially generated fracture networks that collectively represent a variety of distinct characteristics of fracture networks. The main objective is to reveal how these network characteristics qualitatively affect the thermo-mechanical-hydrological behavior of the reservoir, rather than to quantify the performance of specific reservoirs.

4.1 Reservoir Characteristics

We first investigate five distinct fracture networks, Networks B through F, illustrated in Fig. 13. Network A denotes the idealized case introduced in Sect. 3.

A few properties are shared by all of the fracture networks. All networks have the same fracture intensity in terms of total fracture trace length (area in 3D) per unit area (volume in 3D). The initial pore pressure, temperature, and in situ stress of all the reservoirs are the same as those of the baseline case. We also use the same circulation rate, 20 L/s/100 m thick reservoir for all the cases.

Geometrical characteristics of a fracture network in 3D are usually statistically quantified by a rather complex set of parameters (Dershowitz and Einstein 1988). In 2D, the situation is simpler and the main difference between 2D fracture networks is the fracture pattern, namely orientation and length distributions. In Network B, the orientations of fractures follow a uniform distribution within all possible directions, and the concept of “fracture sets” does not apply to this network. If we use a variable θ to denote the orientation of a fracture with respect to the x-axis, θ follows a continuous uniform distribution in the interval

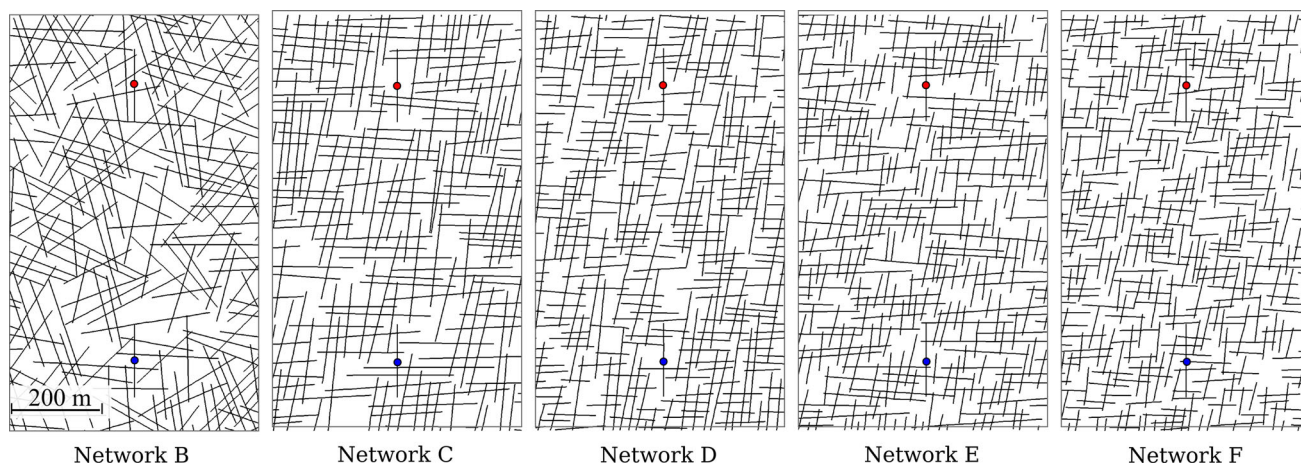


Fig. 13 Fracture connectivity patterns for the five representative fracture networks. Only the center portion of each network is shown. The injection well and production well denoted are 600 m apart, although 400 and 800 m spacings are also investigated

$0^\circ \leq \theta < 180^\circ$. Networks C through F each have two distinct fracture sets. We term the set that is approximately along the north–south direction the “primary set” and the other the “secondary set”, denoted by subscripts “P” and “S”, respectively. The orientations and lengths (l) of each fracture are randomly generated within a specified range. These ranges are provided in Table 2 for all the networks. Note that the fracture generation algorithm enforces the rule that no sub-parallel fractures should intersect with each other. The two sets in Network C have similar fracture lengths. The primary set in Network D has significantly longer fracture than the secondary set, whereas fractures in the secondary set of Network E are significantly longer than those in the primary set. The two sets in Network F have similar fracture lengths, but the fractures are much shorter than those in Network C.

Although all networks have the same fracture intensity, the permeability provided by each network also depends of the connectivity of the fractures, which, to some extent, can be quantified by the average number of fracture–fracture intersections (n_i) on each fracture. The n_i values for all the networks are shown in Table 2. Networks B through E are all well above the percolation threshold (Berkowitz and Ewing 1998), which means that many flow paths can be established within the fracture network between two given points. On the other hand, Network F is barely above the percolation threshold. In order to carry out a “fair comparison”, it is highly desirable to study and compare reservoirs under the same production rate, which requires comparable overall hydraulic impedances. Among other parameters, fracture intensity, fracture orientations, fracture dimension, fracture connectivity, and in situ joint characteristics directly affect the hydraulic impedance of the reservoirs. We choose to alter the joint parameters of

these networks to compensate for the difference in fracture connectivity so that the overall flow impedances are comparable across all scenarios with the same fracture intensity. The current study focuses on reservoir behavior common to all the scenarios evaluated and none of the conclusions to be drawn is a result of the specific joint parameter values. We are primarily concerned with the evolution of flow impedance of each individual scenario, and do not intend to compare the absolute values of flow impedance across different reservoirs. Therefore, the joint parameters used for the different reservoir scenarios do not affect the conclusions reached in this study. The approach taken is analogous to a comparison of actual reservoirs with different fracture connectivities but similar overall hydraulic impedances.

For each network, excluding Network F, we evaluate three inter-well distances: 400, 600, and 800 m. In the case of Network F, only the 600 m inter-well distance is considered. The production well is due north of the injection well. To establish a connection between the wells and the in situ fracture network, we create a hydraulic fracture, running 80 m to the north and to the south of each well. In all other regards, we assume the hydraulic fractures to behave in the same manner as the pre-existing natural fractures. The simulation domain is $2400 \text{ m} \times 2400 \text{ m}$ in size, sufficient for simulating the thermal, hydrological, and mechanical effects of the far field. In Sects. 4.2–4.6, we focus on the scenarios with 600 m inter-well distance and study the effects of well distance in Sect. 4.7.

4.2 Initial Flow Field

The initial flow patterns for the five fracture networks with 600 m well spacing are shown in Fig. 14. The same

Table 2 Characteristics of the five randomly generated fracture networks

	Network B	Network C	Network D	Network E	Network F
Fracture orientation	$0^\circ \leq \theta < 180^\circ$	$75^\circ \leq \theta_p < 85^\circ$ $-5^\circ \leq \theta_s < 5^\circ$	$75^\circ \leq \theta_p < 85^\circ$ $-5^\circ \leq \theta_s < 5^\circ$	$75^\circ \leq \theta_p < 85^\circ$ $-5^\circ \leq \theta_s < 5^\circ$	$75^\circ \leq \theta_p < 85^\circ$ $-5^\circ \leq \theta_s < 5^\circ$
Fracture length	$150 \text{ m} < l < 300 \text{ m}$	$150 \text{ m} < l_p < 300 \text{ m}$ $150 \text{ m} < l_s < 300 \text{ m}$	$150 \text{ m} < l_p < 300 \text{ m}$ $60 \text{ m} < l_s < 120 \text{ m}$	$60 \text{ m} < l_p < 120 \text{ m}$ $150 \text{ m} < l_s < 300 \text{ m}$	$60 \text{ m} < l_p < 120 \text{ m}$ $60 \text{ m} < l_s < 120 \text{ m}$
Fracture connectivity	$n_i = 7.08$	$n_{i_p} = 6.38$ $n_{i_s} = 6.42$	$n_{i_p} = 6.75$ $n_{i_s} = 2.48$	$n_{i_p} = 2.50$ $n_{i_s} = 6.66$	$n_{i_p} = 2.63$ $n_{i_s} = 2.59$
Joint model parameters	$w_{\max} = 1.0 \text{ mm}$ $\sigma_{\text{ref}} = 20 \text{ MPa}$ $w_{\text{ref}} = 0.12 \text{ mm}$	$w_{\max} = 1.0 \text{ mm}$ $\sigma_{\text{ref}} = 20 \text{ MPa}$ $w_{\text{ref}} = 0.12 \text{ mm}$	$w_{\max} = 1.0 \text{ mm}$ $\sigma_{\text{ref}} = 20 \text{ MPa}$ $w_{\text{ref}} = 0.15 \text{ mm}$	$w_{\max} = 1.0 \text{ mm}$ $\sigma_{\text{ref}} = 20 \text{ MPa}$ $w_{\text{ref}} = 0.15 \text{ mm}$	$w_{\max} = 1.0 \text{ mm}$ $\sigma_{\text{ref}} = 20 \text{ MPa}$ $w_{\text{ref}} = 0.3 \text{ mm}$

circulation rate (20 L/s/100 m) is applied to all the networks. The initial pressure drop between injection and production wells for Networks B to F is 7.0, 10.6, 8.3, 12.9, and 10.6 MPa, respectively. As different joint parameters are used for each network, the comparison of these values does not offer much insight into hydraulic behaviors of these networks.

In Network B, the fracture orientations are isotropic, so the concepts of primary and secondary fracture sets are inapplicable. For Network C, the primary set and the secondary set are geometrically similar. However, their apertures are significantly different because the in situ stresses in the x-direction ($\sigma_x = 18 \text{ MPa}$, acting on the y- or primary set fractures) and that in the y-direction ($\sigma_y = 25 \text{ MPa}$, acting on the x- or secondary set fractures) are rather different. These two networks are similar to the baseline regular Network A in the sense that the two fracture sets cannot be differentiated based on geometrical features only. Consequently, the initial flow patterns of these three networks exhibit certain similarities: Flow tends to concentrate in fractures along the north–south direction. Some secondary set fractures (east–west oriented fractures in Network B) have to be engaged as they are necessary for connecting the primary set fractures together. In Network D, the primary-set fractures are longer than the secondary-set fractures and on average each primary-set fracture intersects 6.74 secondary-set fractures while each secondary fracture intersects 2.48 primary-set fractures. Flow in a primary set fracture in Network D can travel a relatively long distance without having to diverge into secondary set fractures. Meanwhile, flow in a secondary fracture does not need to travel a long distance to flow into another primary set fracture. Therefore, the active flow paths in Network D do not spread as wide as those in Network C in the east–west direction. The situation in Network E is the opposite and consequently, the active flow paths spread more widely in the east–west direction than those in Networks C and D. Network F is a special

scenario with low fracture connectivity that is barely above the percolation threshold. Apart from flow to and from the far field, there is only one major flow path between the two wells. Although this flow path splits at some points along the way, the branches soon merge back into a single path. All the five initial flow networks have significant peripheral flow through the far field network.

4.3 Reservoir Performance Without TM Coupling

If we ignore the TM coupling for the sake of understanding the impact of channelized flow, we can use NUFT alone to calculate the responses of the reservoirs during heat production. The production temperature evolution for all the six fracture networks, including the regular grid discussed in Sect. 3, is shown in Fig. 15. Note that simulations ignoring TM coupling only have conceptual significance, since TM coupling always takes place in a real reservoir. However, we can use the results as a proxy for characterizing the diffusivity of the initial flow network, and the results are consistent with a visual assessment of Fig. 14: flow paths in Network B and those in Network C have comparable diffusivity, and these two reservoirs have similar thermal performance; flow paths in Network D are slightly more concentrated than those in Network C, and its thermal performance is moderately worse; Network E has the most diffuse flow paths among all the six scenarios and it also has the longest lasting thermal performance. Network A and Network F have similar thermal performance that is significantly worse than that of the other four scenarios. Although they are at the two ends of the percolation number (i.e. fracture connectivity) spectrum, they share one common characteristic: the flow field is dominated by a single flow path. For Network A, it is the fracture directly connecting the two wells; for Network F, only one viable flow path between the two wells can be established besides peripheral flow paths. The flow path in Network A has much lower hydraulic impedance than that in Network F,

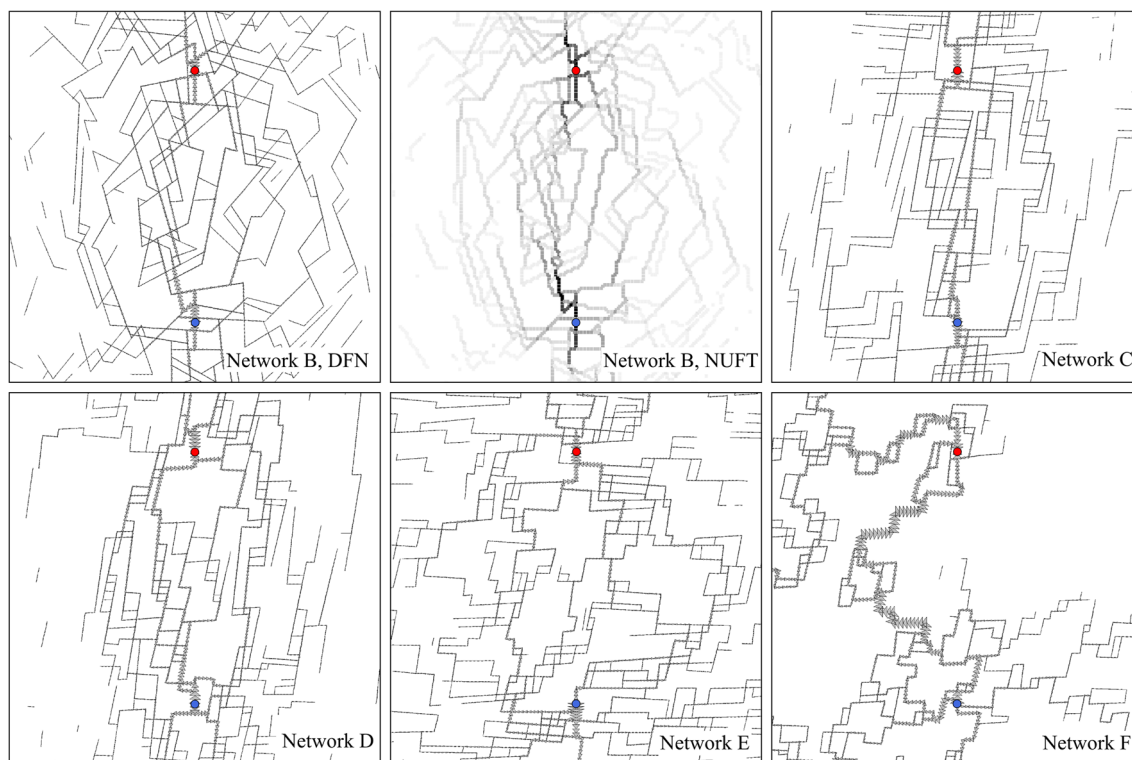


Fig. 14 Initial flow pattern in the five random fracture networks with 600 m well distance. Fractures with flow rate smaller than 0.2 L/s are not shown. For Network B, flow patterns obtained by both the DFN

solver and NUFT are shown. In the NUFT result for Network B, porous medium cells with higher flow rate are rendered darker

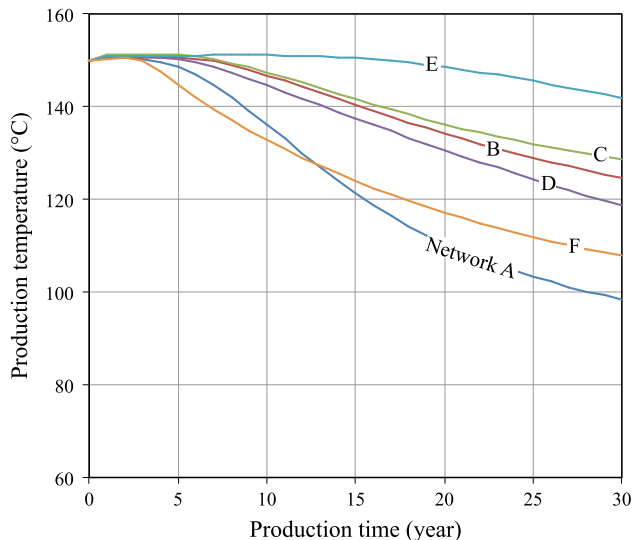


Fig. 15 Production temperature evolution without TM coupling for the six fracture Networks (A–F) with an inter-well separation distance of 600 m

but this difference only affects the overall hydraulic impedance of the reservoirs, not the thermal performance without TM coupling.

The temperature distribution in the reservoirs after 20 years (TM effects ignored) of production is shown in

Fig. 16. The shapes of the cooled zones are consistent with the flow fields: if the flow paths spread wide along the east–west direction, the corresponding cooled zone is also wide. The propagation of the cooling front is slower towards the production well if the cooled zone is wider, implying more desirable thermal performance. The cooled zones in all five simulated reservoirs extend significantly southwards due to the peripheral flow.

4.4 Reservoir Behavior With TM Coupling

The production temperature of the five random fracture networks calculated by THM coupled simulations is shown in Fig. 17 along with the results for Network A. The temperature and flow fields after 2.5, 5, 10, 20, and 30 years of production at the constant circulation rate of 20 L/s are shown in Fig. 18. The injection well and production well are 600 m apart in all the results of the current section.

The most striking observation when we compare the results in Fig. 17 with those in Fig. 15 is the rapid temperature decline in all cases after thermal breakthrough. In Fig. 18 we see that in each reservoir as the cooling front propagates towards the production well, flow always concentrates in a small number of fractures in the cooled zone,

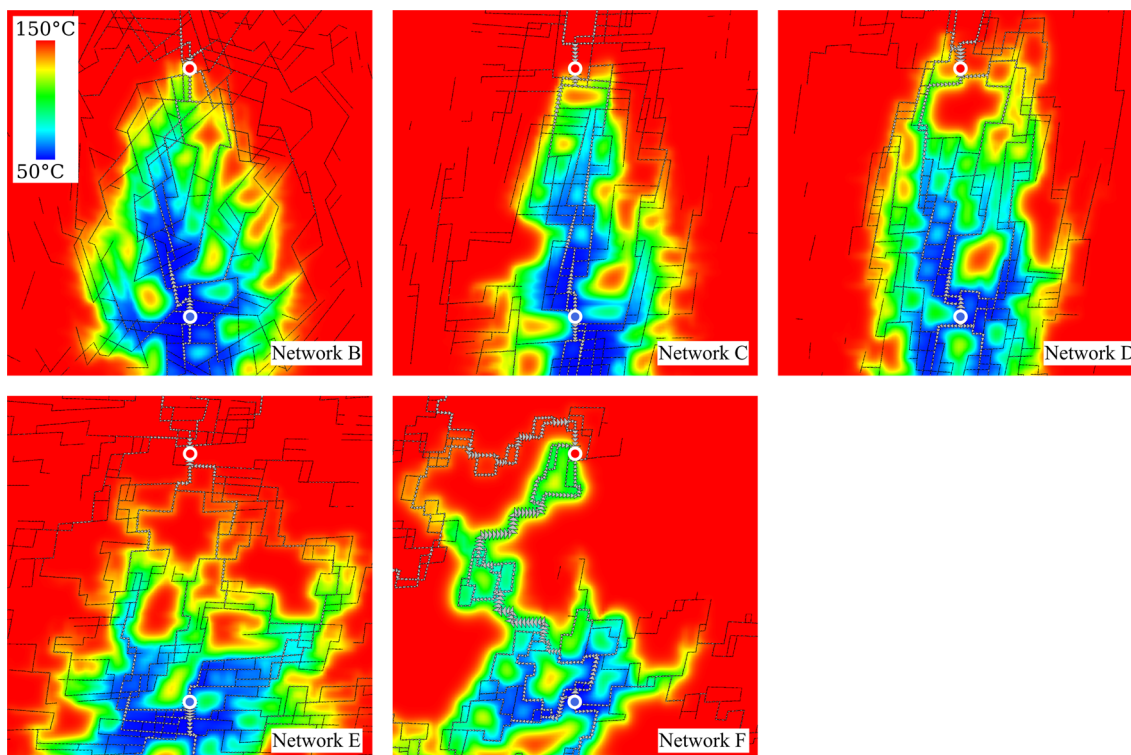


Fig. 16 Reservoir temperature field without TM coupling after 20 years of production. The initial flow fields are overlaid onto the temperature field

regardless of how dispersed the initial flow network had been. The TM effect always impedes peripheral flow, in a fashion similar to that demonstrated in Sect. 3, due to the compressive hoop thermal stress around the cooled zone. This effect further increases the severity of the flow channeling.

Among all the fracture networks, Network E has the most diffuse initial flow pattern, owing to the lack of direct flow pathways connecting the two wells. As a result, the thermal breakthrough in Network E takes place significantly later than that in other networks. Nevertheless, flow channeling into the cooled zone is inevitable. Because the cooled zone does not extend straight between the two wells, Network E has longer flow paths after thermal breakthrough than those in the other networks. This results in a more gradual production temperature decline than that in the networks with shorter flow paths.

Network F is a special case with a low fracture connectivity that is barely above the percolation threshold. The TM coupling only has a moderate effect on the flow field in this fracture network, because there is only one viable flow path between the two wells in the interior of the reservoir. The TM effects tend to decrease hydraulic impedance of the interior portion of the reservoir and reduce peripheral flow, but the change of overall flow pattern is much less substantial than that for Networks B through E. Therefore,

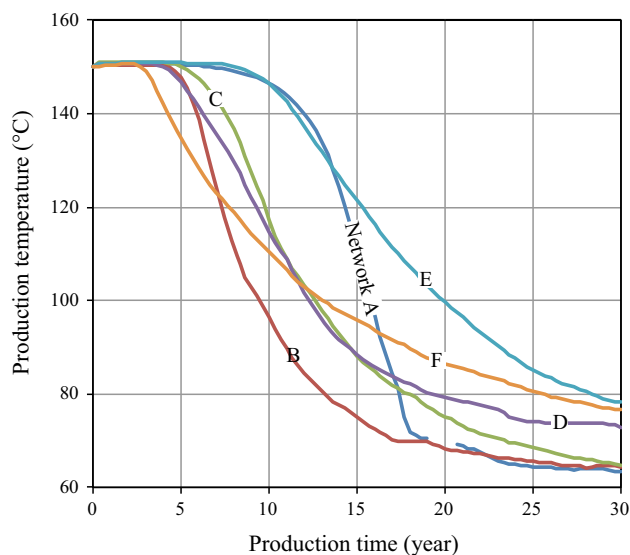


Fig. 17 Production temperature evolution with TM coupling for the six fracture Networks (A–F) with an inter-well separation distance of 600 m

thermal breakthrough takes place in Network F the earliest among all networks, because the flow pattern is the least diffuse, but the temperature decline is more gradual than that of other networks, because a relatively long flow path is retained between the two wells. The decline in

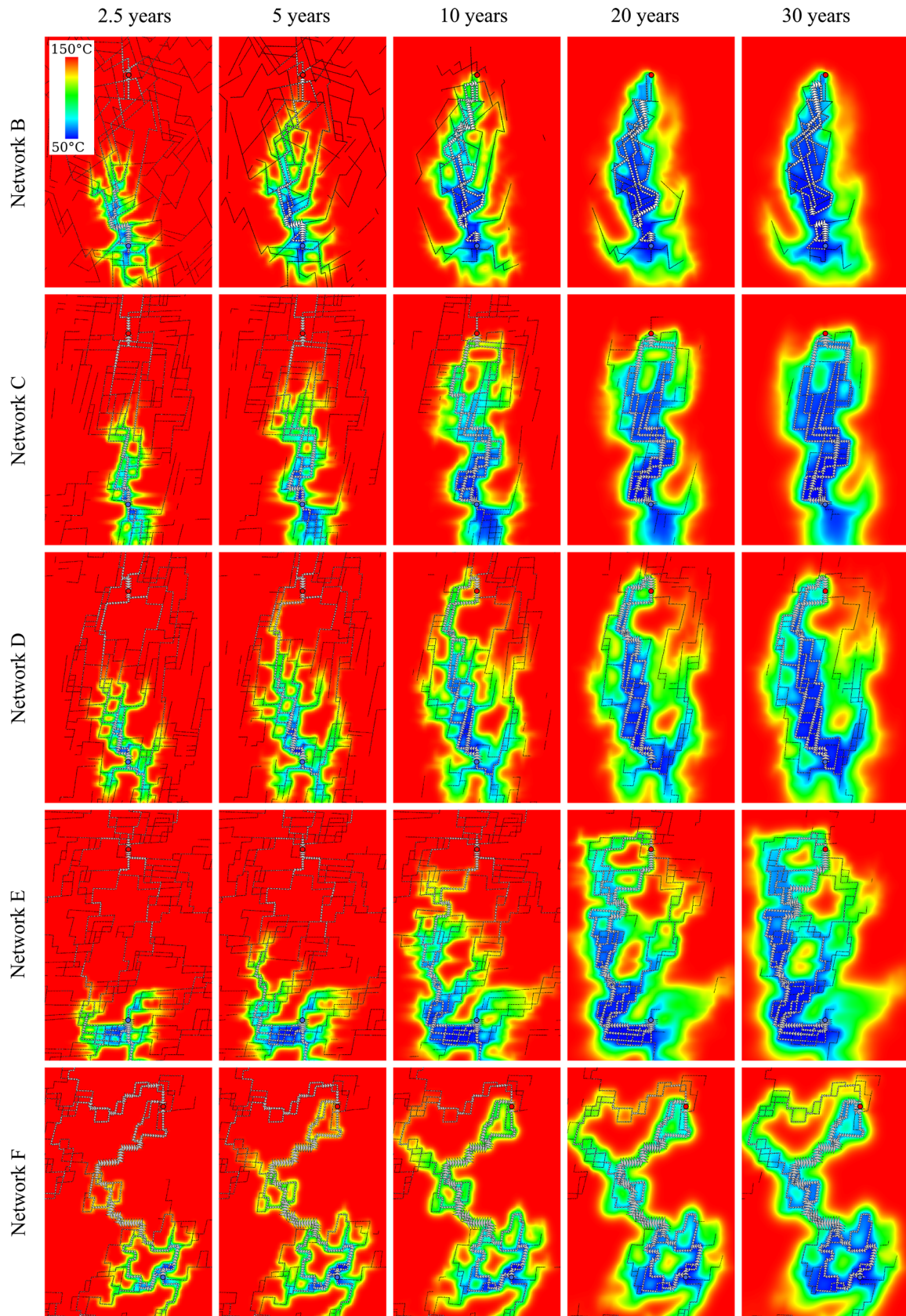


Fig. 18 Temperature and flow fields of in the five random fracture networks during production. Inter-well distance is 600 m for all cases shown

production temperature from Network F is also relatively gradual for a similar reason: the topological characteristics of this reservoir do not allow for a short (and straight) flow path to form between the two wells.

Geometrical and topological characteristics of the fracture network have profound effects on thermal performance of a reservoir. Note that all networks we studied so far have the same fracture intensity. Fracture aperture width mainly affects the reservoir hydraulic impedance while its effects on flow field patterns are insignificant. Therefore, the observed differences are mainly caused by the differences in fracture geometry and topology. Generally speaking, networks with more diffuse initial flow patterns (e.g. Network E) tend to have later thermal breakthrough. However, the TM effects, which dictate the flow pattern evolution during heat production, are highly dependent on characteristics of the fracture network in a rather complex way.

4.5 The Evolution of Overall Hydraulic Impedance

As reservoir temperature decreases, the overall hydraulic impedance between the two wells is expected to decrease owing to less compressive total stress, and thereby smaller effective stress on the fractures. This phenomenon has been observed in real world EGS reservoirs (Kohl et al. 1995). Figure 19 shows the evolution of overall hydraulic impedance of each reservoir with respect to production time, where ΔP is the pressure difference between the two wells and the subscript “0” denotes the initial state. By comparing Figs. 19 with 17 we conclude that the reduction of hydraulic impedance is highly correlated with the decline of production temperature, which is a proxy for overall reservoir temperature. A special case is Network A where the impedance first decreases and then moderately increases between year 1 and 7. This is believed to be caused by the compressive thermal stress at the periphery of the cooled zone, which tends to tighten the fractures. This phenomenon is only observable on Network A but not the other networks, likely due to the unique feature of Network A that much of the permeability in the reservoir is provided by the fracture directly connecting the two wells.

4.6 The Effects of Random Realizations

So far we only generated one random realization for each set of fracture network characteristics. To evaluate whether the results and conclusions are sensitive to random realizations, we generate five additional realizations for Network B and simulate the fluid circulation and heat production with THM coupling. Figure 20 shows the initial flow field and the flow and temperature fields after 20 years of heat production at 20 L/s/100 m thick reservoir for these

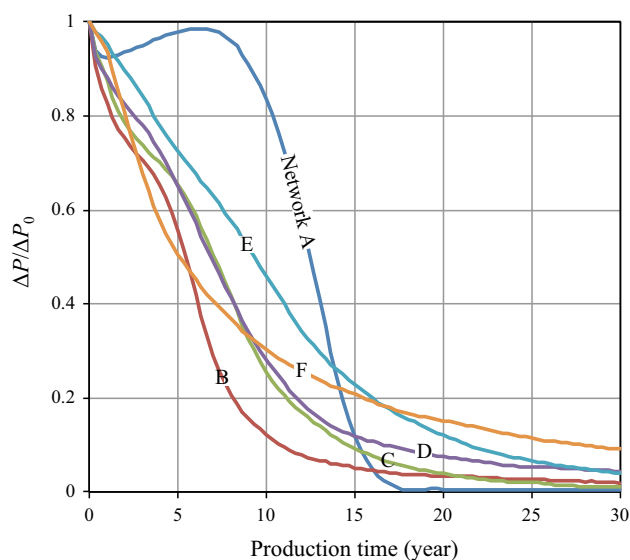


Fig. 19 Evolution of hydraulic impedance for the six simulated reservoirs (A–F) with a 600 m inter-well separation distance

five random realizations. The evolution of production temperature for these five realizations (“Realization 1” to “Realization 5”) along with that for the Network B realization in Sect. 4.2 (“Realization 0”) is shown in Fig. 21.

Although the production temperature evolution curves of the six realizations span a relatively wide range, the variation does not call into question any of the observations in Sect. 4.4 as summarized below.

1. All the six curves show rapid post-breakthrough temperature decline.
2. The networks with more diffuse initial flow patterns (e.g. Realizations 3 and 4) have later thermal breakthrough than those with more concentrated initial flow fields do.
3. Figure 21 compares the production temperature curves of the six Network B realizations with those of Network E and Network F. We argued in Sect. 4.4 that the heat production characteristics of Networks E and F are rooted in their respective fracture network features: Network E’s late breakthrough and gradual post-breakthrough temperature decrease are caused by the lack of direct short connections between the two wells and the abundance of tortuous flow paths, whereas Network F’s early breakthrough and relatively slow post-breakthrough temperature decrease are the results of the low percolation number. Although the six realizations of Network B show a relatively wide range of variation in heat production characteristics, they still share many characteristics that are distinctly different from those of Networks E and F. The thermal breakthrough time of all the six Network B realizations is later than that of Network F but earlier than that of

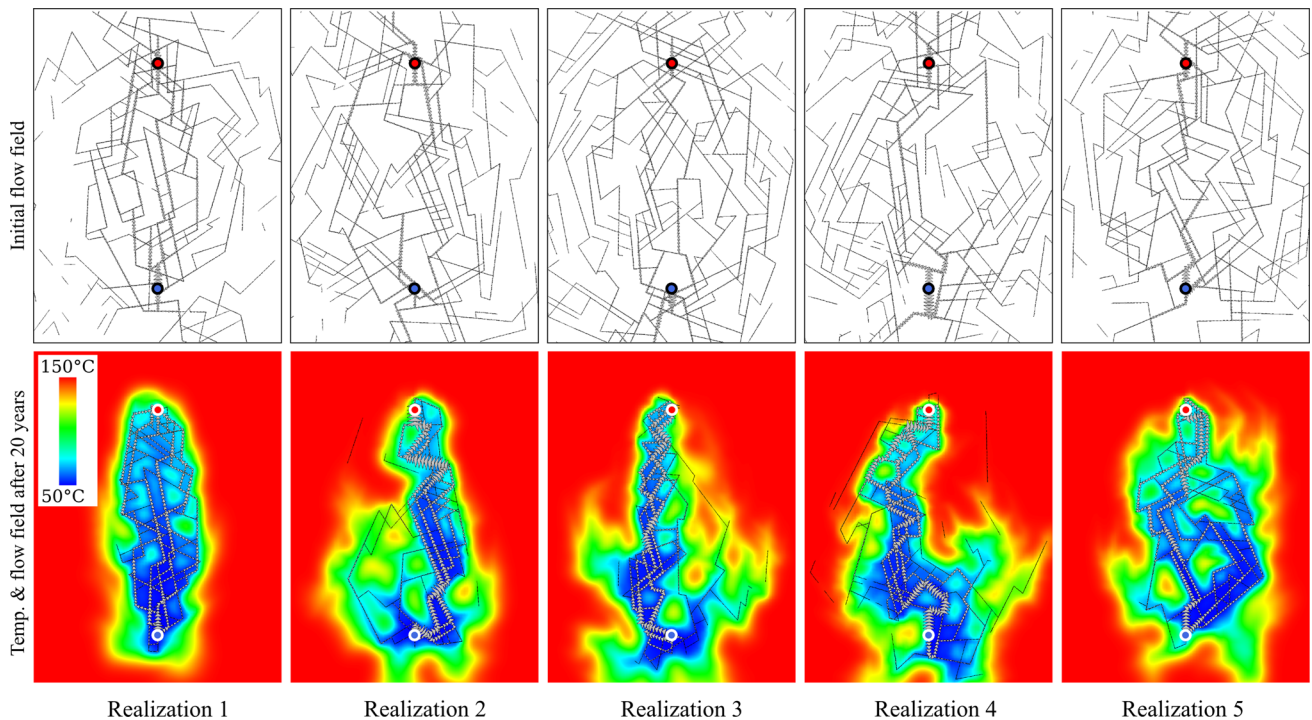


Fig. 20 Five additional random realizations with statistical characteristics identical to Network B. The *images* in the upper row show the initial flow field, and those in the lower row show the flow field and reservoir temperature field after 20 years of production

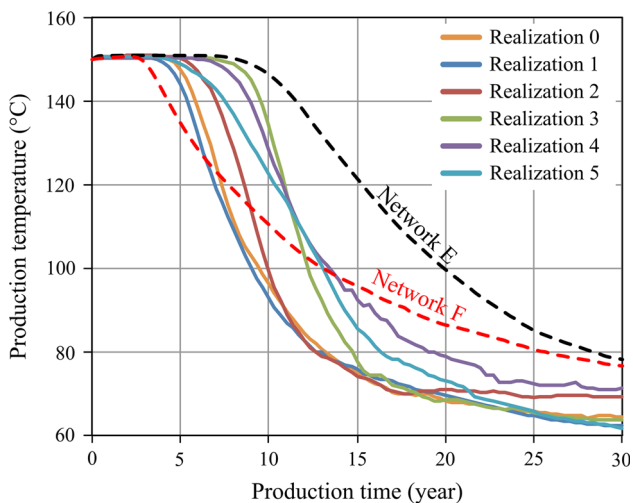


Fig. 21 Production temperature histories of six random fracture network realizations with the same statistical characteristics as Network B. The results of Networks E and F are also shown for comparison

Network E. Their post-breakthrough temperature decrease is significantly faster than those of Networks E and F. This proves that the different behaviors of the networks discussed in Sect. 4.4 are indeed primarily caused by the distinct statistical characteristics of the networks, not merely reflecting the random nature of the problem.

4.7 The Effects of Well Distance

Intuitively, increasing the well distance should increase the extractable heat by enlarging the accessible reservoir volume while potentially requiring greater pumping effort. To study these effects, we perform simulations with well distances of 400 and 800 m in addition to the 600 m well distance simulations for Networks B, C, D, and E. One stochastic realization is generated for each combination of well distance and network characteristics, except that multiple realizations of Networks B and E at well distances of 600 and 800 m are included to evaluate the effects of the random process that creates the fracture networks. The injection-extraction pressure drop in the initial state for different fracture networks is summarized in Fig. 22. Each column of data point(s) represents a combination of well distance and fracture network characteristics. Multiple data points are shown for those combinations (Networks B-600 m, B-800 m, E-600 m, and E-800 m) with a series of stochastic realizations.

The effects of well distance on flow impedance do not seem to be definitive. For the combinations with multiple realizations, increasing the well distance seems to increase the total impedance of the system, but the random variation of the results is also very substantial. A closer inspection of individual fracture network characteristics reveals that the observed variation of flow impedance is heavily affected

by the number of natural fractures intersecting the hydraulic fractures connecting to the wells, particularly those connecting to the production well. This factor is not controlled in the randomly generated fracture networks.

To compare the thermal performances of different well distances in a concise manner, we plot the production life of each layout at production temperatures above 145 and 100 °C in Fig. 23a and b, respectively. The flow field and temperature field after 20 years of production are shown in Fig. 24. Overall, the effects of well distance on thermal performance of the reservoir are very significant. For Networks B, C, and D, the percentage of production life increase is greater than the percentage of the increase of well distances. In other words, the production life of each fracture network increases much more than 50 % when the well distance increases from 400 to 600 m, and life increases much more than 33 % when the well distance increases from 600 to 800 m. The baseline realization of Network E shown in Fig. 18 is an anomalous case, as the layout of 800 m well distance has slightly worse thermal performance than the layout with 600 m well distance. In the 600 m layout, the fracture connectivity, especially that near the injection well, dictates that flow paths connecting the two wells in a relatively direct manner cannot form, resulting in long flow paths. In contrast, the 800 m well

distance layout for Network E happens to produce less-tortuous connections between the two wells. Although this small anomaly does not affect the validity of the aforementioned overall trend of the effects of well distance, it reemphasizes the fact that in a random fracture network the inter-fracture connectivity and fracture-well connectivity play a remarkable role in determining behavior of the reservoir.

4.8 The Effects of Fracture Intensity

The fracture intensity in all the above simulations is constant (0.1 m fracture length per m² area in 2D) across all the fracture networks generated. We investigate the effects of increased fracture intensity in the current section. We generate random fracture Network G with the same fracture orientation and length distributions as those in Network C while the fracture intensity has been increased by 67 %. We also generate Network H based on Network E in a similar fashion. The injection well and production well are 600 m apart for both cases. For a given fracture length and orientation distribution, the inter-fracture connectivity increases as fracture intensity increases. $n_{i,p}$ and $n_{i,s}$ are 10.47 and 10.57, respectively for Network G, and 4.11 and 11.03, respectively for Network H. The joint model

Fig. 22 Injection-extraction pressure drop in the initial state for different fracture networks and various inter-well separation distances

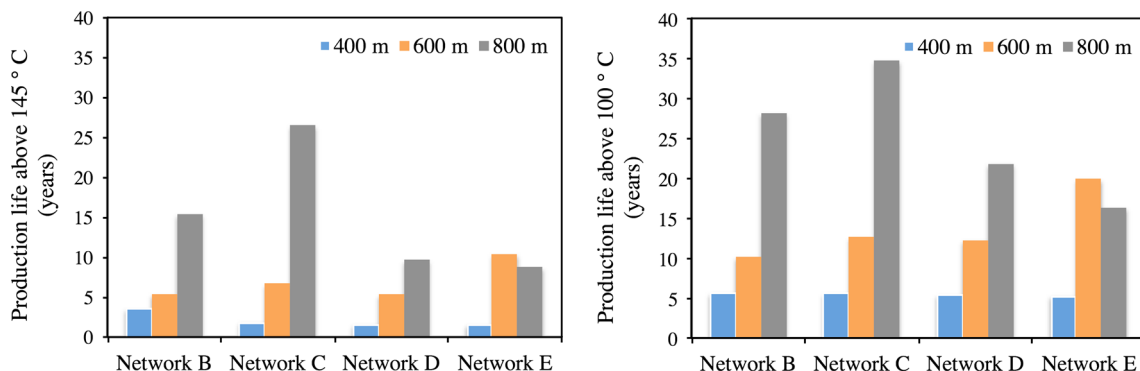
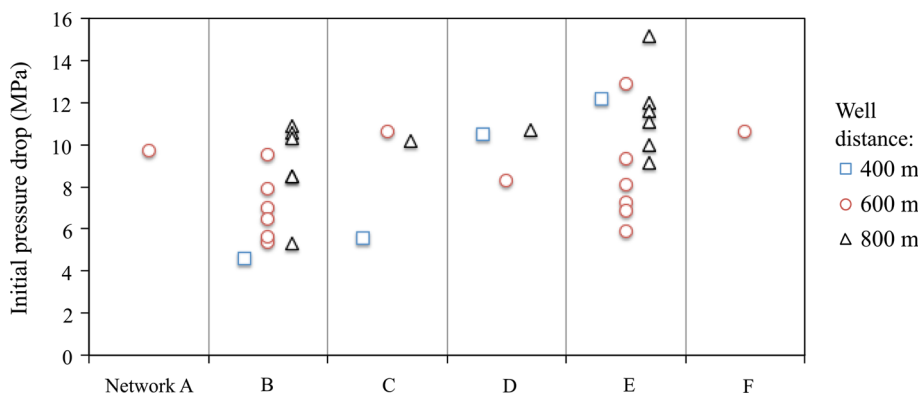


Fig. 23 Reservoir production life at temperature above 145 °C and above 100 °C for different fracture networks and inter-well separation distances

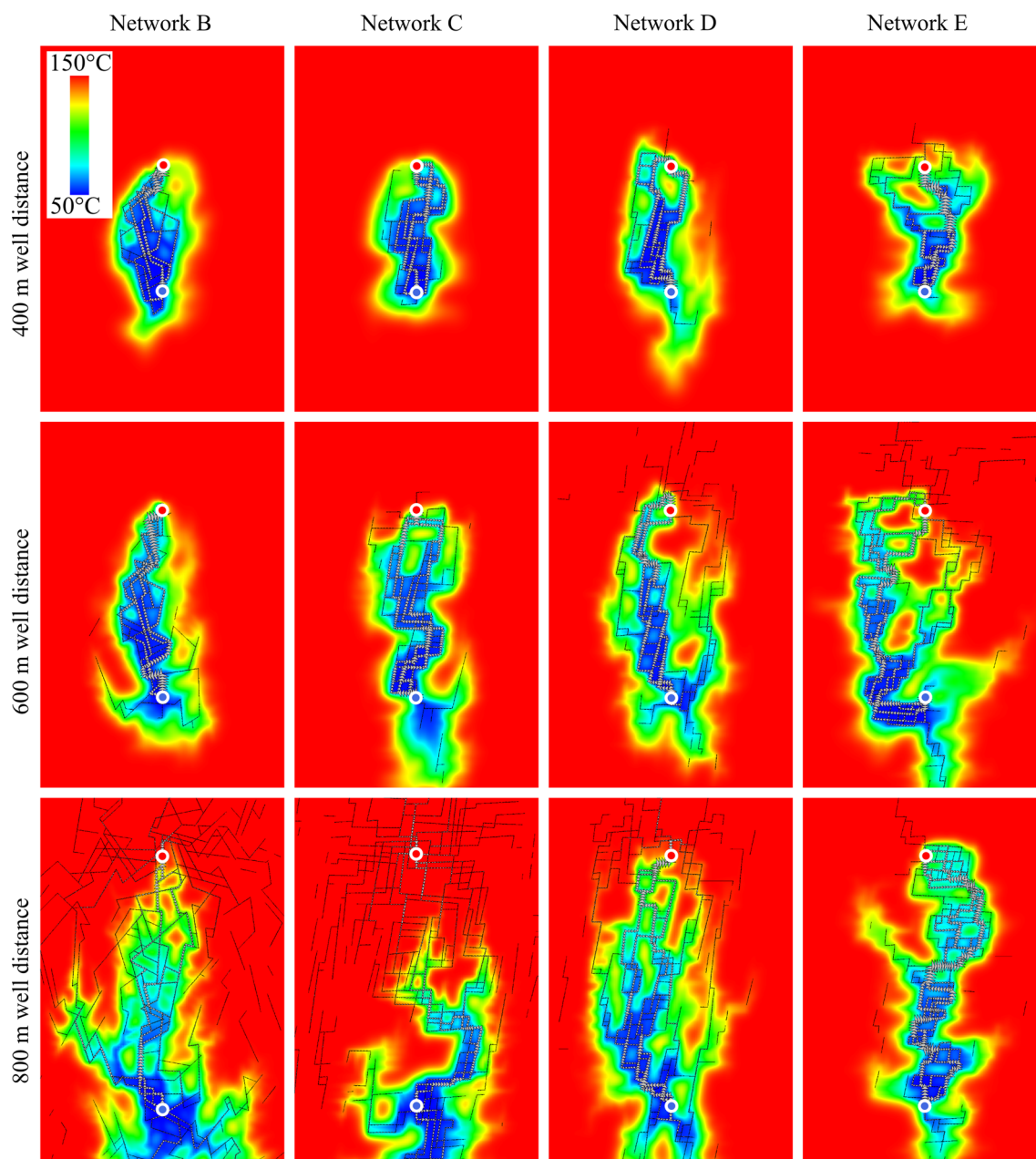


Fig. 24 Reservoir fracture flow field and reservoir temperature field for different fracture Networks (B, C, D, and E) and inter-well separation distances (400, 600, and 800 m) after 20 years of production

parameters for Networks G and H are the same as those for Networks C and E, respectively. At the same circulation rate of 20 L/s, the initial pressure difference between the injection well and the production well is 3.13 MPa for Network G, and 2.91 MPa for Network H, much lower than the values for their low fracture intensity counterparts, which is a direct result of the lower per-fracture flow rate.

Figure 25 shows the initial flow network patterns for these two reservoirs. When flow in Network G is compared with Network C (shown in Fig. 14) and H compared with E (shown in Fig. 14), an expected consequence of the

increased fracture intensity is that flow distributes into more fractures with each fracture carrying a smaller flow rate. However, the overall flow patterns of Networks G and H resemble those of C and E, respectively. As explained in Sect. 4.3, NUFT simulation results without TM effects can be used as a proxy for the degree of flow path diffusivity. With the TM effects disabled, the evolution of production temperature for Networks G and H is shown in Fig. 26a, compared with the results of their low fracture intensity counterparts (TM also disabled). Networks G and H perform slightly worse than Networks C and E, respectively.

This is caused by the high fracture intensity networks' ability to form less-tortuous flow paths than the low fracture intensity networks can. Nevertheless, the difference is small.

The THM coupled simulation results are shown in Figs. 26b and 27. The cooled zone of a high fracture intensity reservoir tends to be more consolidated into the core of the reservoir than its low fracture intensity counterpart. The thermal performance of Network G is comparable to that of Network C. The difference of thermal performance between Networks H and E is remarkable. Recall that the good thermal performance of Network E is mainly caused by the lack of flow pathways directly connecting the two wells, which is combined effect of network features and the particular well locations. The higher fracture intensity in Network H allows much more direct (i.e. straight) flow paths to form.

5 Concluding Remarks and Practical Implications

The current study investigates the effects of thermo-mechanical (TM) coupling on the performance of geothermal reservoirs in discrete fracture networks, with a particular focus on the phenomenon of flow channeling. A series of discoveries and observations have been made through a systematic investigation.

In addition to confirming the well-known flow channeling mechanism, where flow concentrates into a small number of flow paths inside the cooled zone, our numerical simulation reveals a new TM mechanism that counteracts flow channeling to some extent. This secondary mechanism is related to the anisotropy in thermal stress caused by the typically elongated cooling zone. Although the effects of the secondary mechanism are not strong enough to significantly alter the fate of flow channeling, it is possibly an

Fig. 25 Initial flow patterns of Networks G and H

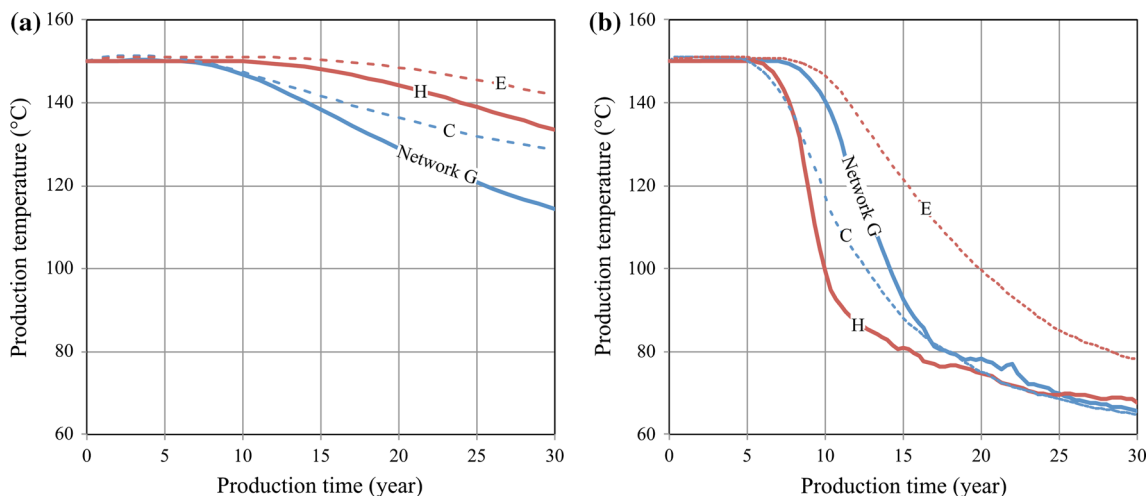
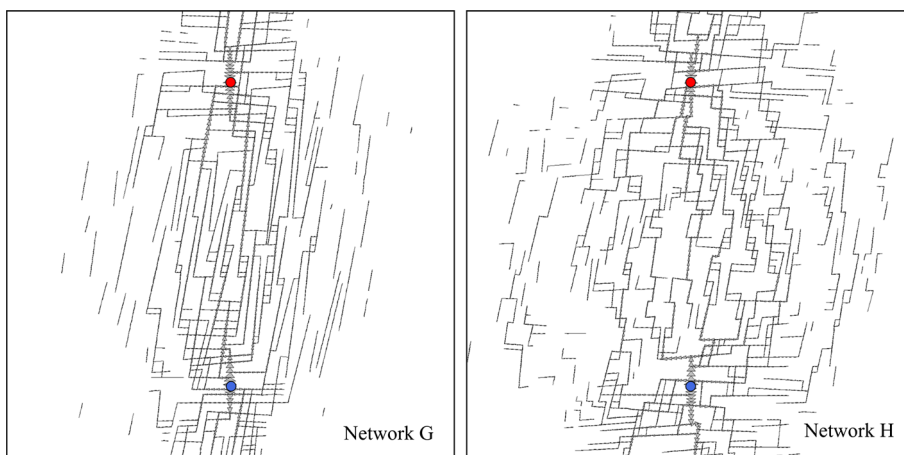


Fig. 26 The evolution of production temperature for high fracture intensity scenarios for a simulations without TM effects and b with TM effects. The comparison with the low fracture intensity counterparts is included

important factor contributing to the temporarily more diffuse flow pattern suggested by tracer tests after some time of production at Fenton Hill (DuTeaux et al. 1996).

Flow channeling seems to be inevitable in all of the fracture networks simulated with TM coupling, despite the wide variety of network characteristics under consideration. The effects of flow channeling on the pre-breakthrough production life is modest. However, flow channeling causes very rapid production temperature decline after thermal breakthrough, thereby severely undermining the economic value of a post-breakthrough reservoir. One reason for the rapid post-breakthrough temperature drop is that the TM effects cause tensile stress increments inside the cooled zone and compressive hoop stresses along the periphery of the cooled zone, which dramatically impedes peripheral flow and eliminates fluid flow's access to the exterior hot rock body. We did not consider spatial variation of fracture properties in the paper, although in real reservoir fractures in some regions could be tighter than those in other regions. However, the phenomenon that fractures carrying higher flow rate cool the surrounding rock faster and flow tends to concentrate more in the cooled zone is universally true, because it is a result of simple thermal–mechanical coupling.

The current study highlights the important role of fracture connectivity in determining the general behavior and

thermal performance of a fractured reservoir. Intensively inter-connected fractures offer low hydraulic impedance and consequently low pumping cost, but also enable the formation of direct flow paths between the two wells, which is a negative factor for reservoir thermal performance. As long as fractures in the network are well interconnected, increasing or decreasing fracture intensity has no significant and consistent effect on effective production life, although it does significantly affect the overall hydraulic impedance of the system. Although the available analysis does not point to specific network characteristics that “optimize” reservoir performance, the current study does highlight the importance of gaining deeper knowledge on this subject.

For a given fracture system, it appears that the only apparent way to effectively prolong the effective production life is to place the two wells further apart. It is interesting to observe that the overall hydraulic impedance is not sensitive to well distance changes, and the modest effect of well distance is often overshadowed by the random nature of fracture networks.

Finally, we acknowledge that it would be inappropriate to directly use our 2D model to quantitatively predict actual reservoir performance. 3D fracture geometries and flow fields are necessarily more complex than those in 2D. However, the flow channeling and accelerated production

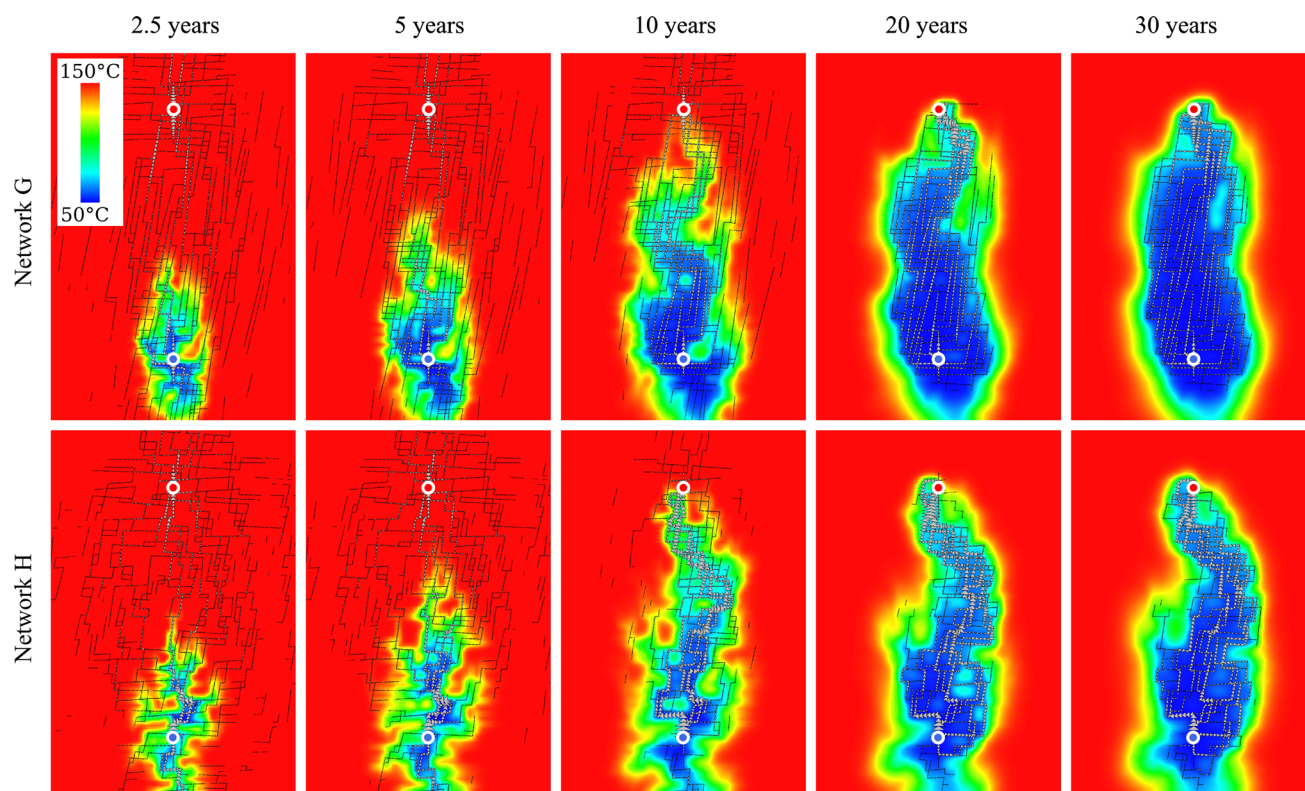


Fig. 27 Temperature and flow fields of in the two random fracture Networks (G and H) with high fracture intensity during production. Inter-well separation distance is 600 m in both cases

temperature decline phenomena revealed and investigated in the current study are direct consequences of two simple physical processes: (1) the aperture and transmissivity of rock joints increases as effective stress decreases, and (2) the cooling of a finite zone causes tensile thermal stress within the cooled zone and compressive hoop thermal stress in the surrounding medium. These two processes are true for both 2D models and 3D reservoirs alike. Therefore, we believe that the discoveries in the current paper apply, at least qualitatively, to real world reservoirs.

Acknowledgments The authors gratefully acknowledge the Geothermal Technologies Office of the US Department of Energy for support of this work. Additional support was provided by the LLNL LDRD project “Creating Optimal Fracture Networks” (#11-SI-006). An anonymous editor of the journal provided valuable advice that substantially improved the quality of this paper, for which the authors are especially grateful. This work was performed under the auspices of the US Department of Energy by Lawrence Livermore National Laboratory under Contract DE-AC52-07NA27344. This paper is LLNL report LLNL-JRNL-644453.

References

- Auradou H, Drazer G, Boschan A, Hulin J-P, Koplik J (2006) Flow channeling in a single fracture induced by shear displacement. *Geothermics* 35:576–588
- Bandis S, Lumsden A, Barton N (1983) Fundamentals of rock joint deformation. *Int J Rock Mech Min Sci Geomech Abstr* 20:249–268
- Barton N, Bandis S, Bakhtar K (1985) Strength deformation and conductivity coupling of rock joints. *Int J Rock Mech Min Sci Geomech Abstr* 22:121–140
- Berkowitz B, Ewing R (1998) Percolation theory and network modeling applications in soil physics. *Surv Geophys* 19:23–72
- Bödvarsson GS, Tsang CF (1982) Injection and thermal breakthrough in fractured geothermal reservoirs. *J Geophys Res* 87:1031–1048
- Botros FE, Hassan AE, Reeves DM, Pohl G (2008) On mapping fracture networks onto continuum. *Water Resour Res* 44:W08435
- Bower K, Zyvoloski G (1997) A numerical model for thermo-hydro-mechanical coupling in fractured rock. *Int J Rock Mech Min Sci Geomech Abstr* 34:1201–1211
- Bruel D (2002) Impact of induced thermal stresses during circulation tests in an engineered fractured geothermal reservoir. *Oil Gas Sci Technol* 57:459–470
- Cook NGW (1992) Natural joints in rock: mechanical, hydraulic and seismic behaviour and properties under normal stress. *Int J Rock Mech Min Sci Geomech Abstr* 29:198–223
- Cook RD, Malkus DS, Plesha ME, Witt RJ (2001) Concepts and applications of finite element analysis. Wiley, New York
- Dershowitz WS, Einstein HH (1988) Characterizing rock joint geometry with joint system models. *Rock Mech Rock Eng* 21:21–51
- DuTeaux R, Swenson D, Hardeman B (1996) Insight from modelling discrete fractures using GEOCRACK. In: Proceedings of the 21st Workshop on Geothermal Reservoir Engineering, SGP-TR-151, Stanford CA, pp 287–293
- Engelder T, Lash GG, Uzcátegui RS (2009) Joint sets that enhance production from Middle and Upper Devonian gas shales of the Appalachian Basin. *Am Assoc Pet Geol Bull* 93:857–889
- Fu P, Carrigan CR (2012) Modeling responses of naturally fractured geothermal reservoir to low-pressure stimulation. In: Proceedings of the 36th Annual Meeting of Geothermal Resources Council, Reno NV
- Fu P, Johnson SM, Carrigan CR (2012) Using explicitly coupled hydro-geomechanical test bed to study hydraulic reservoir stimulation with low pressure. In: Proceedings of the 37th Stanford Geothermal Workshop, Stanford CA
- Fu P, Johnson SM, Carrigan CR (2013) An explicitly coupled hydro-geomechanical model for simulating hydraulic fracturing in arbitrary discrete fracture networks. *Int J Numer Anal Meth Geomech* 37(14):2278–2300
- Genter A, Cuenot N, Goerke X, Melchert B, Sanjuan B, Scheibert J (2012) Status of the Soultz geothermal project during exploitation between 2010 and 2012. In: Proceedings of the 37th Workshop on Geothermal Reservoir Engineering, Stanford CA, SGP-TR-194
- Genter A, Cuenot N, Melchert B, Moeckes W, Ravier G, Sanjuan B, Sanjuan R, Scheiber J, Schill E, Schmittbuhl J (2013) Main achievements from the multi-well EGS Soultz project during geothermal exploitation from 2010 and 2012. European Geothermal Congress 2013, Pisa Italy
- Ghassemi A, Tarasovs S, Cheng AHD (2007) A 3-D study of the effects of thermomechanical loads on fracture slip in enhanced geothermal reservoirs. *Int J Rock Mech Min Sci* 44:1132–1148
- Hao Y, Fu P, Johnson SM, Carrigan CR (2012) Numerical studies of coupled flow and heat transfer processes in hydraulically fractured geothermal reservoirs. In: Proceedings of the 36th Annual Meeting of Geothermal Resources Council Reno NV
- Hao Y, Fu P, Carrigan CR (2013) Application of a dual-continuum model for simulation of fluid flow and heat transfer in fractured geothermal reservoirs. In: Proceedings of the 38th Stanford Geothermal Workshop, Stanford CA
- Hart RD, St. John CM (1986) Formulation of a fully-coupled thermal-mechanical-fluid flow model for non-linear geologic systems. *Int J Rock Mech Min Sci Geomech Abstr* 23:213–224
- Hicks TW, Pine RJ, Willis-Richards J, Xu S, Jupe AJ, Rodrigues NEV (1996) A hydro-thermo-mechanical numerical model for HDR geothermal reservoir evaluation. *Int J Rock Mech Min Sci Geomech Abstr* 33:499–511
- Hogarth RA, Bour D (2015) Flow performance of the Habanero EGS closed loop. In: Proceedings of World Geothermal Congress 2015, Melbourne, Australia, 19–25 Apr 2015
- Jung R (2013) EGS-Goodbye or back to the future. In: Bunger AP, McLennan J, Jeffrey R (eds) Effective and sustainable hydraulic fracturing. InTech, pp 95–121
- Koh J, Roshan H, Rahman SS (2011) A numerical study on the long term thermo-poroelastic effects of cold water injection into naturally fractured geothermal reservoirs. *Comput Geotech* 38:669–682
- Kohl T, Evansi K, Hopkirk R, Rybach L (1995) Coupled hydraulic thermal and mechanical considerations for the simulation of hot dry rock reservoirs. *Geothermics* 24:345–359
- Kresse O, Weng X, Gu H, Wu R (2013) Numerical modeling of hydraulic fractures interaction in complex naturally fractured formations. *Rock Mech Rock Eng* 46:555–568
- McClure MW, Horne RN (2014) An investigation of stimulation mechanisms in enhanced geothermal systems. *Int J Rock Mech Min Sci* 72:242–260
- Mindlin R, Cooper H (1950) Thermoelastic stress around a cylindrical inclusion of elliptic cross-section. *J Appl Mech Trans ASME* 17:265–268
- Nicol D, Robinson B (1990) Modelling the heat extraction from the Rosemanowes HDR reservoir. *Geothermics* 19:247–257
- Nitao JJ (1998) Reference manual for the NUFT flow and transport code version 2.0. Lawrence Livermore National Laboratory, Livermore CA

- O'Sullivan MJ, Pruess K, Lippmann MJ (2001) State of the art of geothermal reservoir simulation. *Geothermics* 30:395–429
- Reeves DM, Benson DA, Meerschaert MM (2008) Transport of conservative solutes in simulated fracture networks: 1 synthetic data generation. *Water Resour Res* 44:W05404
- Rutqvist J, Wu YS, Tsang CF, Bodvarsson G (2002) A modeling approach for analysis of coupled multiphase fluid flow heat transfer and deformation in fractured porous rock. *Int J Rock Mech Min Sci* 39:429–442
- Settgast RR, Johnson SM, Walsh SDC, Fu P, Ryerson FJ (2012) Simulation of hydraulic fracture networks in three-dimensions. In: *Proceedings of the 37th Stanford Geothermal Workshop*, Stanford CA
- Taron J, Elsworth D (2009) Thermal–hydrologic–mechanical–chemical processes in the evolution of engineered geothermal reservoirs. *Int J Rock Mech Min Sci* 46:855–864
- Taron J, Elsworth D, Min KB (2009) Numerical simulation of thermal-hydrologic-mechanical-chemical processes in deformable fractured porous media. *Int J Rock Mech Min Sci* 46:842–854
- Tsang C, Neretnieks I (1998) Flow channeling in heterogeneous fractured rocks. *Rev Geophys* 36:275–298
- Tsang YW, Tsang CF (1987) Channel model of flow through fractured media. *Water Resour Res* 23:467–479
- Willis-Richards J, Watanabe K, Takahashi H (1996) Progress toward a stochastic rock mechanics model of engineered geothermal systems. *J Geophys Res* 101:17481–17496